Individual Project – Final Report 2019-2020

Numerical Modelling of Thermal Management Systems for Lithium-ion Batteries

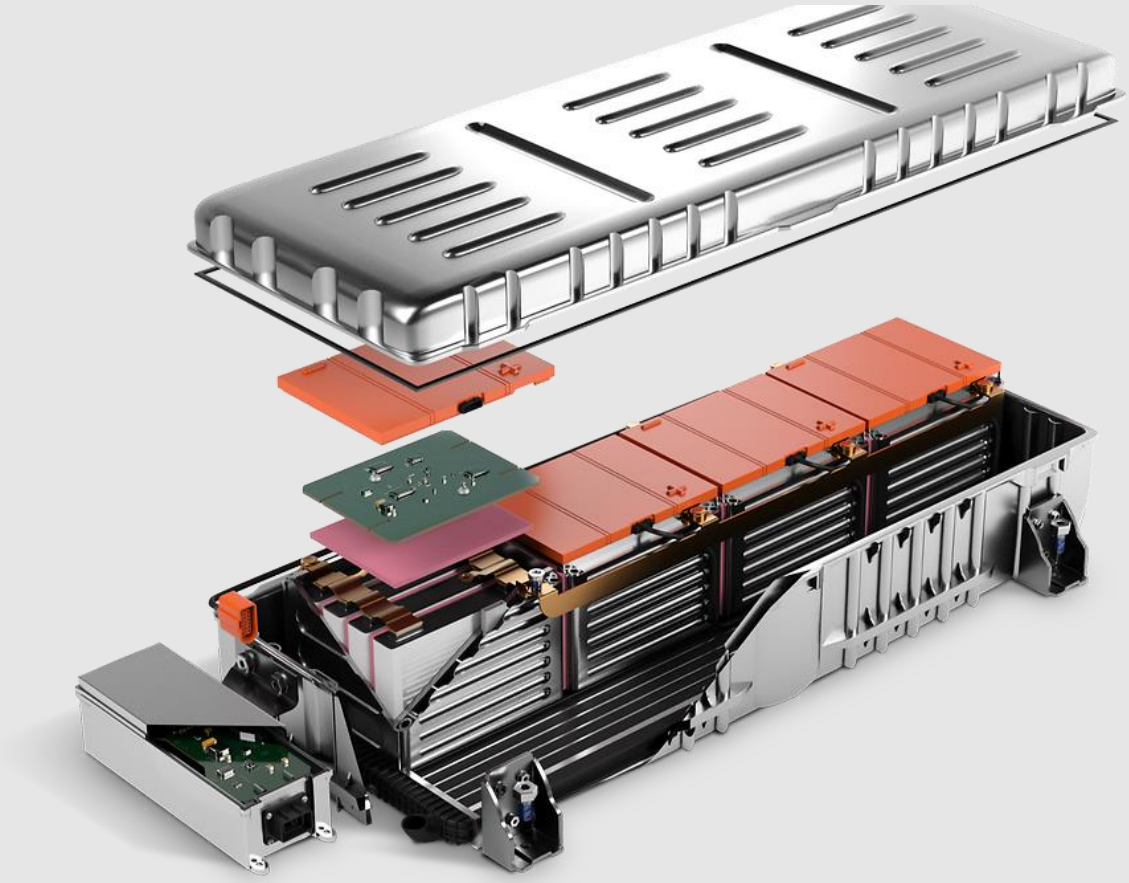

MANCHESTER 1824
The University of Manchester

Omar Elsewify 10189937

A dissertation submitted to The University of Manchester for the degree of BEng Mechanical Engineering in the Faculty of MACE

Acknowledgments

I would like to thank Dr Masoud Jabbari for being my project supervisor and for his continuous support throughout this project. I am grateful for his feedback, enthusiasm and technical direction. I also appreciate the opportunity to be a member of the Complex Flow Group led by Dr Jabbari. It has been a pleasure and a great learning experience.

Abstract

As the automotive industry has shifted its focus towards electric-powered vehicle development, the demand for effective Li-ion battery cells has surged. To reach optimal performance levels these modern batteries function at higher and narrower operating temperature ranges. These conditions present significant obstacles for design engineers; they must tackle greater safety risks, shorter battery lives, and hindered efficiencies amongst other power problems. Research has been undertaken to investigate how an effective cooling system can be utilized to prevent overheating and to ensure heat dissipation away from the battery cells. These cooling systems are part of what is known as a Battery Thermal Management System (BTMS).

A numerical model of the Li-ion batteries found in electric vehicles is developed and the effectiveness of different thermal management systems is assessed. MATLAB is used for simulating the heat flux into and out of a 2-dimensional battery cell. The code is marched through time. Different boundary conditions are set, representative of varying thermal management systems, including submersion of the cell in Phase-Change Material, use of an internal cooling channel, and use of graphene nanoparticle to increase cell thermal conductivity.

The numerical model developed in this project was validated against experimental data from the open literature and was found to be accurate in predicting maximum temperature to within 96%. Results agree with the experiment and show high peak temperatures over the recommended range under some conditions. The model was adapted to simulate the effect that BTM systems would have on the thermal patterns found in the cell. Results show that by adopting a combination of these systems, the maximum temperature can drop by over 40%. An optimal solution is presented which is effective and practical in meeting the cooling demands and is an amalgamation of two BTMS systems.

INTELLECTUAL PROPERTY STATEMENT

The author of this dissertation (including any appendices and/or schedules to this dissertation) owns certain copyright or related rights in it (the "Copyright") and s/he has given The University of Manchester certain rights to use such Copyright, including for administrative purposes.

Copies of this dissertation, either in full or in extracts and whether in hard or electronic copy, may be made only in accordance with the Copyright, Designs and Patents Act 1988 (as amended) and regulations issued under it or, where appropriate, in accordance with licensing agreements which the University has entered into. This page must form part of any such copies made.

The ownership of certain Copyright, patents, designs, trademarks and other intellectual property (the "Intellectual Property") and any reproductions of copyright works in the dissertation, for example graphs and tables ("Reproductions"), which may be described in this dissertation, may not be owned by the author and may be owned by third parties. Such Intellectual Property and Reproductions cannot and must not be made available for use without the prior written permission of the owner(s) of the relevant Intellectual Property and/or Reproductions.

Further information on the conditions under which disclosure, publication and commercialisation of this dissertation, the Copyright and any Intellectual Property and/or Reproductions described in it may take place is available in the University IP Policy, in any relevant Dissertation restriction declarations deposited in the University Library, and The University Library's regulations.

Declaration

I declare that this thesis has been composed solely by myself and that it has not been submitted, in whole or in part, in any previous application for a degree. Except where stated otherwise by reference or acknowledgment, the work presented is entirely my own.

TABLE OF CONTENTS

Word Count: 14450
Word Count including footnotes and endnotes: 14498

List of Figures

List of Tables

1 Introduction

1.1 Project Background

1.1.1 Historical Context of Project

Since Jean Joseph Etienne Lenoir first implemented petrol fuel in the internal combustion engine of his three-wheeled carriage in 1863, the automotive industry has become more and more reliant upon the availability of fossil fuels as the power source of their vehicles. This massive reliance upon crude oil is seen in a great spike in global primary energy consumption by fossil fuels consumption over the past century (Smil, 2016).

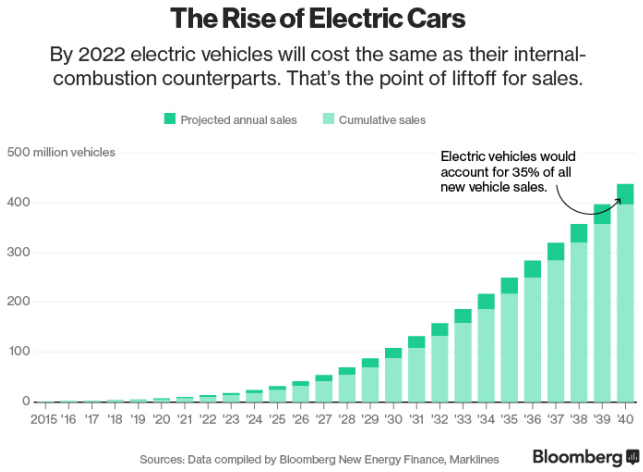

Figure 1 Prediction as to how the demand for electric cars is expected to boom in the coming decades.

This intrinsic dependence upon fossil fuels may no longer be a suitable option for the industry as world reserves are depleting at a rapid unsustainable rate. Some predictions estimate that as early as 2042 the world's crude oil reservoirs will deplete leaving many automotive vehicles without any power (Shafiee and Topal, 2009). In an attempt to forestall and avoid the consequences of this crisis, many automotive companies have begun developing sustainable vehicles which are independent of fossil fuels. Electrically driven vehicles (EDVs) have emerged as the most suitable replacements for petrol cars and almost all automotive firms currently manufacture a commercial EDV or are in the process of developing one for public use. By using electric power instead of fuel, the vehicle's well-to-wheel carbon dioxide emissions reduce drastically. In the case of the Tesla Roadster, the CO_2 levels are roughly 3 times less than the typical petrol engine (Eberhard and Tarpenning, 2006). Figure 1 shows that at this rate of EDV development Bloomberg New Energy Finance predicts that by 2040, more than a third of new production cars will be electric (Randall, 2016).

The first mass-produced commercial vehicle that utilised electric batteries was the Toyota Prius, which was released in 1997. The Prius' design was a hybrid vehicle making use of both electric battery cells and gasoline as power sources for motion. The design was initially met with complaints regarding aesthetics and spaciousness, however, later models addressed this and the car became one of the most successful vehicles in history (Halbright and Dunn, 2010). The next step was mass-producing fully electric vehicles, which Tesla accomplished in 2006, by introducing the Tesla Roadster which ran on an AC induction motor using lithium-ion battery cells. This car was the first commercially marketed and mass-produced fully electric vehicle but was more of a novelty than a practical car for the public.

1.1.2 Current Problems Facing the EDV Industry

Most of the current obstacles facing EDV development are attributed to the properties of the battery cells used, these include mileage, cycle life, charging time, safety and reliability (Deng et al., 2018). Of the currently available batteries, the one with the greatest potential for success is the lithium-ion (Li-ion) battery which outperforms the others with regards to specific energy, specific power, cell voltage and self-discharge rate (see Table 1) (Liu et al., 2017).

Table 1 Properties of different electric vehicle batteries (Liu et al., 2017)

Type	Specific Energy (Wh/kg)	Specific Power (kW/kg)	Nominal Cell Voltage (V)	Life cycles	Self-discharge rate (%)
Lead-acid	25-40	150-250	2	200-700	5
Nickel-iron	50	100	1.2	2000	20-40
Li-ion	110-180	300	3.6	>1000	10

However, one of the biggest challenges associated with Li-ion power is that the operating temperature range is very narrow and there are significant safety risks that appear when functioning outside this range. When temperatures exceed 80°C thermal runway becomes a concern, as it causes harmful gas emissions, smoke, fires and possible explosions (Deng et al., 2018). Furthermore, when the temperature gradient is outside 5°C there are detrimental effects on battery longevity and exacerbated degradation of the cells (Worwood et al., 2017).

The heat generated within the cells is a function of the charging and discharging processes and these impact the batteries' capabilities, reducing these rates would solve some issues but limit the maximum power output. As such, one of the main focuses of EDV research is the development of thermal management systems to cool the battery cells to within the optimal range. This helps overcome the safety and longevity concerns while drastically improving performance and simultaneously maintaining the same level of power output.

1.2 Aims and Objectives

This project aims to investigate the effectiveness of different thermal management systems, and to compare their performances to find an optimal solution for EDV. The project will develop a numerical model to represent an EDV Li-ion battery in 2 dimensions. The code should be able to model the effect of time on the heat dissipation as well as produce temperature vs time plots at distinct locations on the battery surface.

Objectives:

- Find an optimal operating setup which reduces the maximum temperature and temperature gradients while also allowing for a high-power output
- Provide context for how the optimal setup will improve performance (i.e. the effect on maximum power output, battery life)
- Make a reasonable supported conclusion as to which optimum cooling system the electric car industry should adopt moving forward.

1.3 Research Questions

- To what extent does the use of battery thermal management systems affect the heat distribution within the cell and how can this affect the battery's performance.
- How can the modification of certain cooling systems parameters improve cooling effectiveness?
- How can an optimal solution be constructed which provides the greatest cooling while maintaining an even temperature gradient?

1.4 Project Impact

The work undertaken in this project will be of benefit to the electric driven automotive industry, as it will present evidence as to how to optimise the thermal management system of battery cells in their vehicles. This information will help in optimising the power performance and longevity of the EDVs produced.

The research will benefit the environment as it potentially will reduce the likelihood of thermal runway, which will lead to reduced greenhouse emissions and a more sustainable mode of transport. Additionally, by helping to design the cooling system effectively the research will possibly increase EDV production and help outnumber the traditional environmentally unfriendly vehicles on the road.

The research will also benefit society in that the improvements in longevity will increase the appeal of electric vehicles to consumers who were hesitant to purchase the vehicles because of their shortcomings. Society will also benefit through the increased safety that comes with the effective cooling, as the chance of battery overheating, or explosion will be reduced.

2 Literature Review

2.1 Current Context of Project

There are currently two fundamental issues that the electric vehicle must overcome to attain top performances. Firstly, there are functionality concerns; overheating of the power cells is commonplace and so is the shortage of battery life. Secondly, there are also significant safety concerns; thermal runaway regularly happens, and battery explosions are rare but pose a deadly risk to the public (Liu et al., 2019).

Because of the thermal context of these concerns, Li-ion battery manufacturers often quote optimal/safe operating temperatures such as to minimize the risk of the aforementioned concerns. The window of recommended operating temperatures for most automotive batteries varies between each manufacturer but also varies between the different stages of the battery cycle: for discharging, -20 to 55°C, and for charging, 0 to 45°C (Lu et al., 2013). The operating voltage is also kept to a limit of 1.5 – 4.2 V such as to improve reliability (Lu et al., 2013). It is also required that the temperature gradient within a single cell not exceed 5°C as this causes the cell to perform as if it was at higher temperatures than it truly is, this leads to shorter cell life as well damaging the cell structure (Worwood et al., 2017).

These temperature ranges are often hard to maintain while attempting to extract as much energy as possible from the batteries. As such, there has been an abundance of research conducted to investigate the use of thermal management systems that allow for maximum power production while keeping the batteries within an optimal/safe window. These BTM systems have three main tasks (Lu et al., 2013):

1. *Protect the cells and battery packs from being damaged*
2. *Make the batteries operate within the proper voltage and temperature interval, guarantee the safety and prolong their service life as long as possible.*
3. *Maintain the batteries to operate in a state that the batteries could fulfil the vehicles' requirements.*

The thermal management systems that will be investigated in this report will be assessed with regards to how well they accomplish these three tasks.

2.2 Description of Current Thermal Management Systems

2.2.1 Liquid Cooling

Liquid cooling involves using a coolant tank, a radiator and a pump. The system must be connected such that liquid can travel through the radiator and back to the tank. The radiator is positioned near the battery surface such that the heat transfer rate can be maximised. The pump increases the volume flow rate allowing for even larger heat transfer.

Liquid cooling is effective in that it uses a liquid medium, such as water, which has a very high thermal conductivity and specific heat capacity allowing for great temperature reductions at the battery surface (Deng et al., 2018).

However, liquid cooling systems are heavy and take up a lot of space, which is not ideal for commercial use. They also require additional power to activate the pumping mechanism, this power is referred to as parasitic power.

According to research by Hunan University, the liquid cooling system can be optimised using a graphite plate between the battery cell and the radiator pipes, this reduces the temperature difference from 7°C to 2°C (Deng et al., 2018). This is explained by the extremely high thermal conductivity of the graphite plate effectively improving the heat transfer efficiency of the system and increasing the direct contact area between the battery and the radiator pipes. The authors conclude that Novec 7000 cooling fluid is promising as it absorbs large amounts of heat during its boiling process, but because of the availability of water and oil and their low costs, these are the most promising for industry (Deng et al., 2018).

2.2.1.1 Air Cooling

In automotive air cooling, the motion of the car through the air in the atmosphere is used to transfer heat away from the battery. It can be viewed from the perspective that the car is stationary, and that airflow is incoming at a velocity equal to the speed of the car. Channels are built into the structure of the car to allow for airflow to reach the batteries and be exhausted out to the atmosphere.

This system is very lightweight and cost-effective as it does not require the machining or manufacturing of complex structures. It also utilises the motion of the vehicle for forcing convection meaning that parasitic power is kept to a minimum.

On the downside, the air medium has a very low thermal conductivity and low specific heat capacity, so it has a limited cooling performance (Deng et al., 2018).

In a paper comparing BTM systems, by Beijing Jiaotong University, air cooling was used in a cooling loop similar to the liquid cooling setup and it was found that with air much more power was needed to control the maximum temperature than with liquid and jacket cooling (Chen et al., 2016). The paper concluded that because of its high parasitic power consumption and low heat transfer rates, the air is not an effective BTMS. However, freestream air cooling was not considered, this would remove any need for parasitic power it would also improve cooling as the air is not recycled so there is a continuous influx of cool air.

2.2.2 Heat Pipes

Heat pipes are split into three sections, an evaporator and a condenser with an adiabatic section in-between. In the evaporator heat radiated from the battery is absorbed by fluid in the saturated state, this heat is then transferred to the condenser where the heat is lost to a cooling fluid. The fluid is then pulled back to the evaporator through capillary forces and the cycle repeats with heat being transferred away from the battery.

The advantage of using heat pipes is that they are generally lightweight, compact and have flexible geometries (Deng et al., 2018). Furthermore, heat pipes make use of temperature gradients to transfer heat, therefore an external power supply is not needed.

The disadvantage of the heat pipes is that they superimpose a temperature gradient onto the battery, meaning some regions will be of much higher temperature than others which can severely reduce battery lifespan. Furthermore, they require very low coolant temperatures to efficiently transport heat away from the cell.

In a paper by Warwick Manufacturing Group, heat pipes were investigated in a setup where a heat pipe was fitted concentrically within a cylindrical battery. The idea was that in this configuration the imposed temperature gradient can be avoided. However, they concluded that by adding the heat pipes, there was a 5.8% decrease in the energy density of the cell and an 11.7% increase in the cell mass (Worwood et al., 2017). Furthermore, they noted that to increase heat transfer rates to an adequate level, forced convection or liquid cooling is required at the base of the heat pipe.

2.2.3 Phase Change Material

The idea behind using phase change materials (PCM) is that they absorb the latent heat produced by the battery and thus transfers the heat away from the cell itself. The material melts when heated by the battery and freezes back into solid during the off periods.

Essentially, the PCM acts as a heat sink during the battery operation and during inactivity, it serves as a heat source.

Common PCMs are paraffin waxes and hydrated salts both of which provide moderate to large energy storage densities. The two main advantages of the PCM structures is that they are lightweight, and they do not require additional power.

However, the PCMs exhibit very low thermal conductivities which means that a very large surface area is required for effective heat transfer. Also, the PCM system presents design engineers with a difficult encapsulation situation as the materials often do not conform to the available geometry (Farid et al., 2004). Furthermore, during idle/standby the PCM releases energy back to the batteries increasing their temperatures offsetting their main purpose.

In work done by Guangdong University of Technology, a pure PCM model was tested and it was found that with this model the temperature gradient can be consistently maintained under 2°C even at 3C discharge rates (Wu et al., 2017). However, they also found that on its own the PCM cannot keep the temperature within the safe window for prolonged periods. To overcome this a combination of a liquid cooling system and a PCM system was used and it was found that this combination kept the temperature under 50°C for more than 25,000 seconds whereas the pure PCM exceeded 50°C at around 10,000 seconds. Furthermore, by the 25,000-second mark, the pure PCM temperature exceeded 75°C, which would have undoubtedly lead to thermal runaway (Wu et al., 2017).

Commercial phase change materials can be installed as a liquid phase or a solid phase. Typical values for solid PCMs are between 0.1 – 0.35 W/mK, whereas liquid PCMs can range from 1 to 5 W/mK. These values can be increased notably by the addition of graphene nanoparticles.

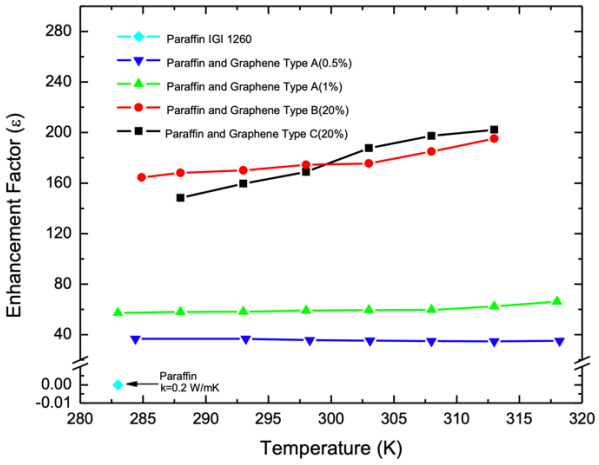

Figure 2 Enhancement Factor of paraffin composites with different graphene fractions (Goli and Balandin, 2014).

This phenomenon is seen in Figure 2, taken from a research paper conducted by the University of California Riverside. A typical commercial pristine paraffin with thermal conductivity of 0.25 W/mK had 1 wt.% of graphene particles added to it, and the thermal conductivity rose to 15 W/mK, an increase by a factor of 60 (Goli and Balandin, 2014). Increasing the graphene content to 20 wt.% produced thermal conductivities of up to 45 W/mK an increase by a factor of more than 200. However, the research paper also noted that increasing the graphene content to such a high extent would increase in the cell outer shell temperature, which in turn would increase the cell temperature within the battery itself.

2.3 Gaps in Literature

After reviewing the current literature available related to the project, a few topics and explorations appear to be lacking, this section addresses these gaps.

- **Effects of tab cooling**
    - By cooling the positive and negative tabs the heat flux into the cell volume is likely to be reduced which would mean that the total heat is decreased. Some research has been conducted with regards to tab dimension optimisation to improve safety (Mei et al., 2018), but work done regarding system implementation at the tabs is sparse.
- **Alternative cooling fluids**
    - Research concerning oil as a cooling fluid for batteries is sparse, mainly because of its very high viscosity, if this problem is addressed it may be the future of BTM systems(Deng et al., 2018). By adding nanoparticles or liquid metal into coolant flows the thermal conductivity of the system is significantly increased. This would maintain relatively the same weight but would allow for greater heat transfer away from the battery.
- **Influence of vehicle velocity on cooling rates**
    - In traditional petrol-powered vehicles, there is extensive research on how microchannels are used to cool the engine block and make use of the incoming airflow velocity. Most electric cars store their batteries at the rear of the car or the middle, to help with weight distribution, but at this point, the airflow is significantly disturbed by the car body, so cooling would be

erratic. It would be of greater benefit if the batteries are placed in front of the car such as to make use of the car's velocity as a cooling system.

- **Effects of nearby cells on heat transfer**
    - For most work done in simulation the model only relates to one cell such as to simplify the numerical calculations. To account for this a heat transfer term is added to the boundary conditions. However, this assumption may not be valid for all batteries if some are cooled significantly more than others. Further research must be done to investigate the effects of the battery setup grid to reach more accurate conclusions.
- **Adjusting the numerical model to resemble experimental reality**
    - The majority of research conducted establishes a numerical simulation from a series of governing thermodynamic equations and modelling formulas. However, no attempts are made to validate the codes being used or to incorporate real-life performance characteristics into the model. This work will attempt to improve the model by accounting for the discrepancies between the simulation results and experimental results collected from previous years.

3 Methodology and Research Design

3.1 Modelling and Simulation

A numerical model is used to simulate the temperature changes in a Li-Ion battery, this model is governed by the two-dimensional heat conduction equation. Although the model is based on the fundamental heat equation it does not completely replicate the cell in reality. To achieve the real-life thermal patterns an experiment must be conducted in a lab, where thermal imaging can capture the results. However, research conducted in this form is much more time consuming and susceptible to external errors, therefore, numerical simulation provides a suitable alternative, particularly if the model is validated using experimental data. Additionally, the computational model allows for easy changes in input parameters and initial conditions such as ambient temperature which are much more difficult to control in reality. Overall, the model must provide sufficiently accurate data while also being efficient and simple to utilise.

3.2 Description of Methodology

3.2.1 MATLAB code development

The focus of this project is the simulation of the physics involved in the discharging of Li-ion cells. To run this simulation, this project looked at developing a numerical model using MATLAB coding. This approach was taken as it allowed for greater control of simulation parameters as well as providing greater flexibility in terms of the approach taken for results procurement. These benefits would not otherwise have been possible through the use of commercial software such as ANSYS Fluent or Abaqus.

<u>MATLAB code development method:</u>

1. Make the following set of assumptions about the battery and the thermodynamics involved to simplify the modelling process:
   - Heat generation is entirely electrothermal, chemical reactions are represented through resistors.
   - Assume no degradation through one cycle of discharging
   - The thermal pattern does not vary in the z-direction (only in x and y direction)
   - Use of a single cell (i.e. no heating effect from surrounding cells)

2. Develop a code to represent the Li-Ion battery geometry as a square mesh of a certain resolution in which the nodes represent certain points on the surface of the cell.
3. Add in boundary conditions to the model to replicate the battery and its positive and negative tabs, (see Figure 3):
    - Constant heat transfer rate at both tabs
    - Heat loss from left, bottom and right sides as well as gaps on the top edge
    - Internal domain has an additional heat generated term
4. Develop a model for the thermal dissipation over time and write the code to represent the time-dependent behaviour of the battery
5. Run a mesh convergence test to ensure grid independence as well as ensure the appropriate use of computing power.
6. Convert heat flux into cell face value temperatures then convert into graphic representation (i.e. temperature contour plot)

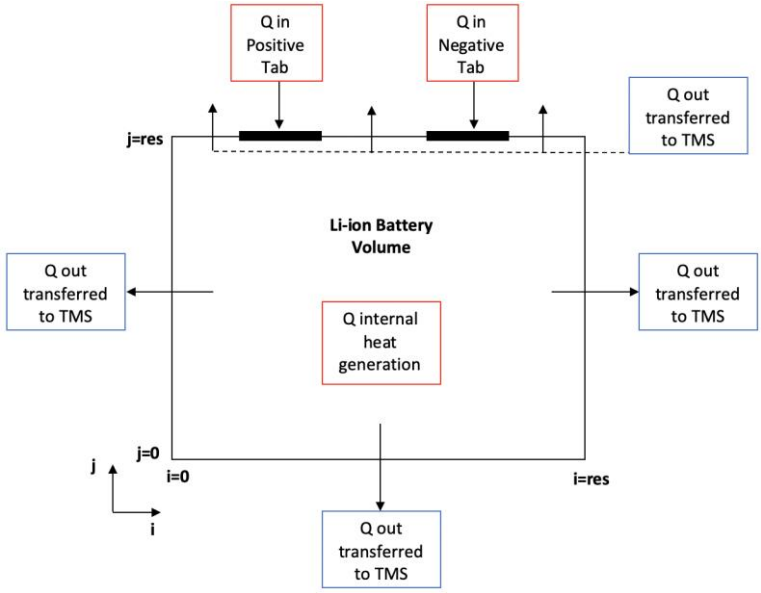

Figure 3 Illustration of Li-ion battery boundary conditions in 2 dimensions

3.2.2 Battery Thermal Management System implementation

The next focus of this project was changing the boundary conditions established in the aforementioned MATLAB code to replicate different thermal management approaches. To do this all the heat out boundary conditions were changed to reflect the BTMS being investigated. One of the challenges faced in this stage was finding accurate values for heat

convection and conduction coefficient terms, to represent certain commercial cooling mechanisms.

Thermal Management System implementation method:

- Change the current and examine the effect this has with regards to the temperature plots produced.
- Consider passive cooling using natural convection and phase changing materials and examine how each affects the thermal distribution in the battery.
- Consider different cooling setups including combinations of two or more cooling kits
- Find an optimal operating setup which reduces the temperature gradient while also allowing for a high-power output

3.2.3 Postprocessing of results and data

The final step of the analysis method employed is the postprocessing of the results produced through the numerical simulation. The validation results produced are to be compared with thermal images from an external experiment, so they must be presented in the same form. Also, the same colour bar and scale must be used to facilitate comparison.

Postprocessing method:

- Produce a coloured contour representing the thermal patterns on the battery surface
- Produce a Temperature vs Time plot representing the temperature changes at a given node on the cell
- Produce a quiver plot representing the magnitude and direction of the heat flux within the cell.

4 Theory

To create the 2D simulation for this project, certain fundamental equations of heat transfer were used along with numerical modelling discretization techniques.

4.1 Heat Transfer Theory

The governing equation for the heat transfer in the battery cell is the unsteady heat conduction equation also known as the Fourier-Biot Equation:

$$\frac{\partial T}{\partial t} = \alpha\left[\frac{\partial^2 T}{\partial x^2} + \frac{\partial^2 T}{\partial y^2}\right] + \frac{\dot{q}''}{\rho c_p} \qquad \text{(Eqn.1)}$$

Where:

ρ is density kg/m^3

c_p is specific heat capacity J/kgK

$\dot{q}''$ is internal heat generation (W/m^3)

α is the thermal diffusivity (m^2/sec) given by $\alpha = \frac{k}{\rho c_p}$

k is the conductive heat transfer coefficient for the cell (W/m^{2}K)

For the initial work of this project the $\frac{\partial T}{\partial t}$ term was nulled, indicating a steady-state problem. However, for the work done after that the $\frac{\partial T}{\partial t}$ term was considered, leading to a time-dependent temperature distribution.

The governing equations for heat transfer away from the cell are the heat convection equation (i.e. Newton's Law of Cooling) and the heat conduction equation (Fourier's Law).

Newton's Law of cooling:

$$q = h\left(T - T_f\right) \qquad \text{(Eqn.2)}$$

Where: q is heat transfer per unit area (W/m^2), h is convective heat transfer coefficient (W/m^{2}K), and T_f is the freestream temperature of the cooling fluid (K).

Fourier's Law

$$q = k\frac{\partial T}{\partial x} \qquad \text{(Eqn.3)}$$

Where: q is heat transfer per unit area (W/m^2), k is conductive heat transfer coefficient (W/m^{2}K), and $\frac{\partial T}{\partial x}$ is the temperature gradient (K/m).

The T value is the temperature of the boundary of the battery just before it comes in contact with the cooling system, in this project, these are the points with i or j values of 1 or res (see Figure 3).

Essentially the greater the temperature difference the greater the heat transfer rate away from the battery. Equation 2 can only be used with the air and liquid systems, which allow for convection and heat transfer away from the battery. Equation 3 can only be used for phase change materials as they are solids in direct contact with the cell.

4.2 Mathematical Model

The whole volume of the cell is governed by Equation 1, and three possible boundary conditions can be applied to the edges of the battery cell (Wang and Ni, 2019):

$$T = \bar{T} \qquad (\in \Gamma_1, t > t_0)$$

$$k\frac{\partial T}{\partial n} = q \qquad (\in \Gamma_2, t > t_0)$$

$$k\frac{\partial T}{\partial n} = h\left(T - T_f\right) \qquad (\in \Gamma_3, t > t_0)$$

Where:

Γ_1 is the Dirichlet (first-type) boundary condition, Γ_2 the Neumann (second-type) boundary condition, Γ_3 is the Robin (third-type) boundary condition,

$\bar{T}$ is the temperature given by the Dirichlet condition,

k is the heat conduction coefficient of the object

q is the heat flux

n is the boundary outer normal vector (x or y)

h the heat convection coefficient of the object

4.3 Time Discretization Theory

The unsteady nature of the heat transfer physics involved means that there must also be a discretization in the time dimension. For this model, the explicit time integration scheme was used. This entails computing a new value of a quantity in the future using the information at the current time (Jabbari, 2019b).

$$\frac{\partial T}{\partial t} = \frac{T_{i,j}^{t+\Delta t} - T_{i,j}^{t}}{\Delta t} \qquad \text{(Eqn.4)}$$

Where:

$T_{i,j}^{t+\Delta t}$ is the temperature at point (i,j) at the new time step

$T_{i,j}^{t}$ is the temperature at point (i,j) at the current time step

Δt is the time step

This scheme steps blindly into the future, and as a result, it is very important to determine a suitable Δt value for the simulation. If the Δt is too large the solution will become unstable and the program will likely crash, also the accuracy is reduced with larger Δt values.

4.4 Spatial Discretization Theory

To solve for the temperature at any point in the battery, the area must be split up into discrete cells and nodes. Depending on what nodal resolution is defined, the number of cells will increase or decrease. For this model i nodes are set in the x-domain and j nodes are set in the y-domain, and h is the grid spacing in the Δx and Δy directions. Once the number of cells is defined, a cell spatial discretization method must be used to solve for the values of each cell. Because the heat transfer equations include a Laplacian function, with second derivates of temperature T in both x and y directions, a finite difference equation can be used to approximate the second-order derivatives. This can be derived from an expansion of the Taylor Series and produces equation (5) when using a 3-point stencil (Jabbari, 2019a). Because of the 2-dimensional nature of the problem a 5-point stencil including centre point and two neighbouring points in both x and y directions is used (Jabbari, 2019a).

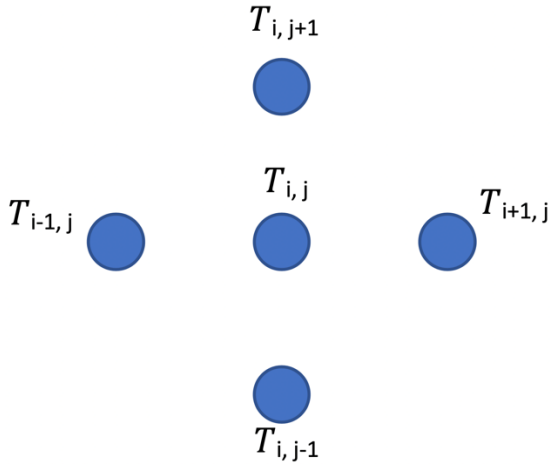

$$\frac{\partial^2 T_{i,j}}{\partial x^2} \approx \frac{1}{h^2}\left(T_{i+1,j} - 2T_{i,j} + T_{i-1,j}\right) \quad \text{and} \quad \frac{\partial^2 T_{i,j}}{\partial y^2} \approx \frac{1}{h^2}\left(T_{i,j+1} - 2T_{i,j} + T_{i,j-1}\right) \quad \text{(Eqn.5)}$$

$$\nabla^2 T_{i,j} = \frac{\partial^2 T_{i,j}}{\partial x^2} + \frac{\partial^2 T_{i,j}}{\partial y^2} = \frac{1}{h^2}\left(T_{i+1,j} + T_{i-1,j} - 4T_{i,j} + T_{i,j+1} + T_{i,j-1}\right) \quad \text{(Eqn.6)}$$

The Laplacian discretization (Eqn.6) then applies at all points except those which are on the boundaries. The discretization in Equation 6 is then combined with Equations 1 and 4 to produce:

$$T_{i,j}^{t+\Delta t} = \frac{\alpha \Delta t}{h^2}\left(T_{i+1,j}^{t} + T_{i-1,j}^{t} - 4T_{i,j}^{t} + T_{i,j+1}^{t} + T_{i,j-1}^{t}\right) + \frac{\dot{q}'' \Delta t}{\rho c_p} + T_{i,j}^{t}$$

The Fourier Number is given as $Fo = \frac{\alpha \Delta t}{h^2}$, so the equation above can be rewritten as:

$$\boldsymbol{T_{i,j}^{t+\Delta t} = Fo\left(T_{i+1,j}^{t} + T_{i-1,j}^{t} + T_{i,j+1}^{t} + T_{i,j-1}^{t} + \left(\frac{1}{Fo} - 4\right)T_{i,j}^{t}\right) + \frac{\dot{q}'' \Delta t}{\rho c_p}} \qquad \textbf{(Eqn.7)}$$

To solve for the nodes on the sides of the battery cell, the Neumann boundary condition Γ_2 must be applied for the tabs and the Robin condition Γ_3 must be applied at the edges. The example below illustrates the boundary on the tabs of the battery cell.

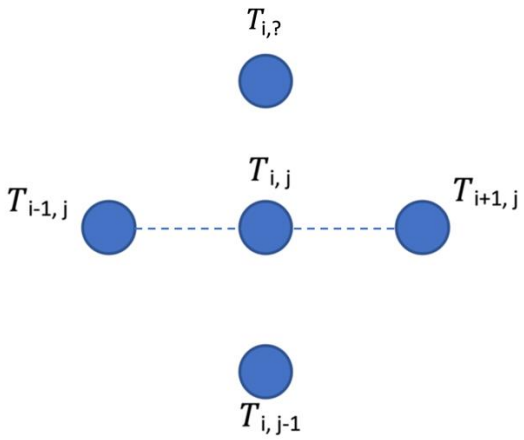

From Equation 7 without internal heat generation (and $T_{i,j+1}^{t}$ becomes $T_{i,?}^{t}$) :

$$T_{i,j}^{t+\Delta t} = Fo\left(T_{i+1,j}^{t} + T_{i-1,j}^{t} + T_{i,?}^{t} + T_{i,j-1}^{t} + \left(\frac{1}{Fo} - 4\right)T_{i,j}^{t}\right)$$

And the Neumann condition states:

$$k_{tab}\frac{T_{i,?}^{t} - T_{i,j-1}^{t}}{2\Delta y} = q \qquad or \qquad T_{i,?}^{t} = T_{i,j-1}^{t} + \frac{2q\Delta y}{k_{tab}}$$

Therefore:

$$\boldsymbol{T_{i,j}^{t+\Delta t} = Fo\left(T_{i+1,j}^{t} + T_{i-1,j}^{t} + 2T_{i,j-1}^{t} + \frac{2q\Delta y}{k_{tab}} + \left(\frac{1}{Fo} - 4\right)T_{i,j}^{t}\right)} \qquad \textbf{(Eqn.8)}$$

Along the sides of the cell the Robin boundary condition Γ_3 is applied, as there is convective heat transfer away from the cell. The example below illustrates the boundary on the right edge of the battery cell.

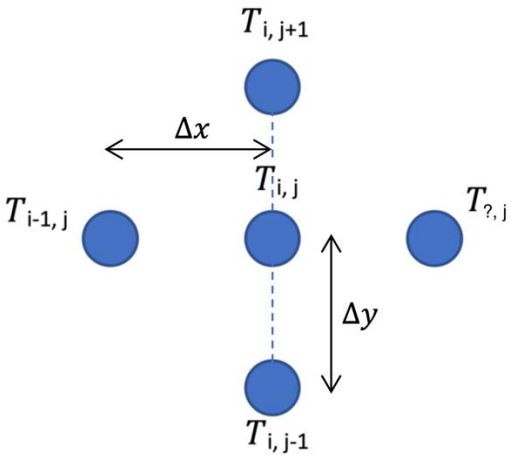

From Equation 7 without internal heat generation (and $T^t_{i+1,j}$ becomes $T^t_{i,?}$):

$$T^{t+\Delta t}_{i,j} = Fo\left(T^t_{?,j} + T^t_{i-1,j} + T^t_{i,j+1} + T^t_{i,j-1} + \left(\frac{1}{Fo} - 4\right)T^t_{i,j}\right)$$

And the Robin condition Γ_3 states:

$$k\frac{T^t_{i-1,j} - T^t_{?,j}}{2\Delta x} = h\left(T^t_{i,j} - T_f\right) \qquad or \qquad T^t_{?,j} = T^t_{i-1,j} - \frac{2h\Delta x}{k}\left(T^t_{i,j} - T_f\right)$$

Therefore:

$$T^{t+\Delta t}_{i,j} = Fo\left(2T^t_{i-1,j} + T^t_{i,j+1} + T^t_{i,j-1} + \frac{2h\Delta x}{k}\left(T_f\right) + \left(\frac{1}{Fo} - 4 - \frac{2h\Delta x}{k}\right)T^t_{i,j}\right)$$

The Biot number is given as $Bi = \frac{h\Delta x}{k}$, so the equation can be rewritten as:

$$\boldsymbol{T^{t+\Delta t}_{i,j} = Fo\left(2T^t_{i-1,j} + T^t_{i,j+1} + T^t_{i,j-1} + 2Bi\left(T_f\right) + \left(\frac{1}{Fo} - 4 - 2Bi\right)T^t_{i,j}\right)} \qquad \textbf{(Eqn.9)}$$

Using different variations of the 4-point stencil, Equation 9 can be adjusted to find the boundary condition equations on the left and bottom edges, as well as the gaps on the top, see Table 2.

Table 2 Discretized boundary condition equations set for an i x j mesh

Location	Unsteady Boundary Condition Equations
Positive tab	$T^{t+\Delta t}_{i,j} = Fo\left(T^t_{i+1,j} + T^t_{i-1,j} + 2T^t_{i,j-1} + \frac{2q\Delta y}{k_{tab_{Pos}}} + \left(\frac{1}{Fo} - 4\right)T^t_{i,j}\right)$
Negative tab	$T^{t+\Delta t}_{i,j} = Fo\left(T^t_{i+1,j} + T^t_{i-1,j} + 2T^t_{i,j-1} + \frac{2q\Delta y}{k_{tab_{Neg}}} + \left(\frac{1}{Fo} - 4\right)T^t_{i,j}\right)$
Empty gaps	$T^{t+\Delta t}_{i,j} = Fo\left(2T^t_{i,j-1} + T^t_{i+1,j} + T^t_{i-1,j} + 2Bi\left(T_f\right) + \left(\frac{1}{Fo} - 4 - 2Bi\right)T^t_{i,j}\right)$

Right Edge	$T_{i,j}^{t+\Delta t} = Fo\left(2T_{i-1,j}^{t}+T_{i,j+1}^{t} + T_{i,j-1}^{t} + 2Bi(T_f) + \left(\frac{1}{Fo} - 4 - 2Bi\right)T_{i,j}^{t}\right)$
Left Edge	$T_{i,j}^{t+\Delta t} = Fo\left(2T_{i+1,j}^{t}+T_{i,j+1}^{t} + T_{i,j-1}^{t} + 2Bi(T_f) + \left(\frac{1}{Fo} - 4 - 2Bi\right)T_{i,j}^{t}\right)$
Bottom Edge	$T_{i,j}^{t+\Delta t} = Fo\left(2T_{i,j+1}^{t}+T_{i+1,j}^{t} + T_{i-1,j}^{t} + 2Bi(T_f) + \left(\frac{1}{Fo} - 4 - 2Bi\right)T_{i,j}^{t}\right)$
Internal Domain	$T_{i,j}^{t+\Delta t} = Fo\left(T_{i+1,j}^{t} + T_{i-1,j}^{t}+T_{i,j+1}^{t} + T_{i,j-1}^{t} + \left(\frac{1}{Fo} - 4\right)T_{i,j}^{t}\right) + \frac{\dot{q}''\Delta t}{\rho c_p}$

The corner nodes of the grid are solved for by averaging the two cells on either side of the corner node.

To model the effect that phase change materials would have on the temperature distribution within the cell, Equation 9 must be modified to model conduction heat exchange as opposed to convection heat exchange.

The Robin boundary condition Γ_3 becomes:

$$k\frac{T_{i-1,j}^{t} - T_{?,j}^{t}}{2\Delta x} = k_{BTMS}\frac{T_{i,j}^{t} - T_f}{\Delta x}$$

Where:

k_{BTMS} is the thermal conductivity coefficient for the thermal management system

T_f is the temperature of the cooling material.

As a result, Equation 9 becomes:

$$\boldsymbol{T_{i,j}^{t+\Delta t} = Fo\left(2T_{i-1,j}^{t}+T_{i,j+1}^{t} + T_{i,j-1}^{t} + \frac{2k}{k_{BTMS}}(T_f) + \left(\frac{1}{Fo} - 4 - \frac{2k}{k_{BTMS}}\right)T_{i,j}^{t}\right)} \quad \textbf{(Eqn.10)}$$

Similar to the convection condition, the temperature terms in Equation 10 can be adjusted to match the stencil associated with the boundary being considered.

4.5 Code Flowchart

The steps described in the Methodology and Research Design section can be depicted by the following flowchart.

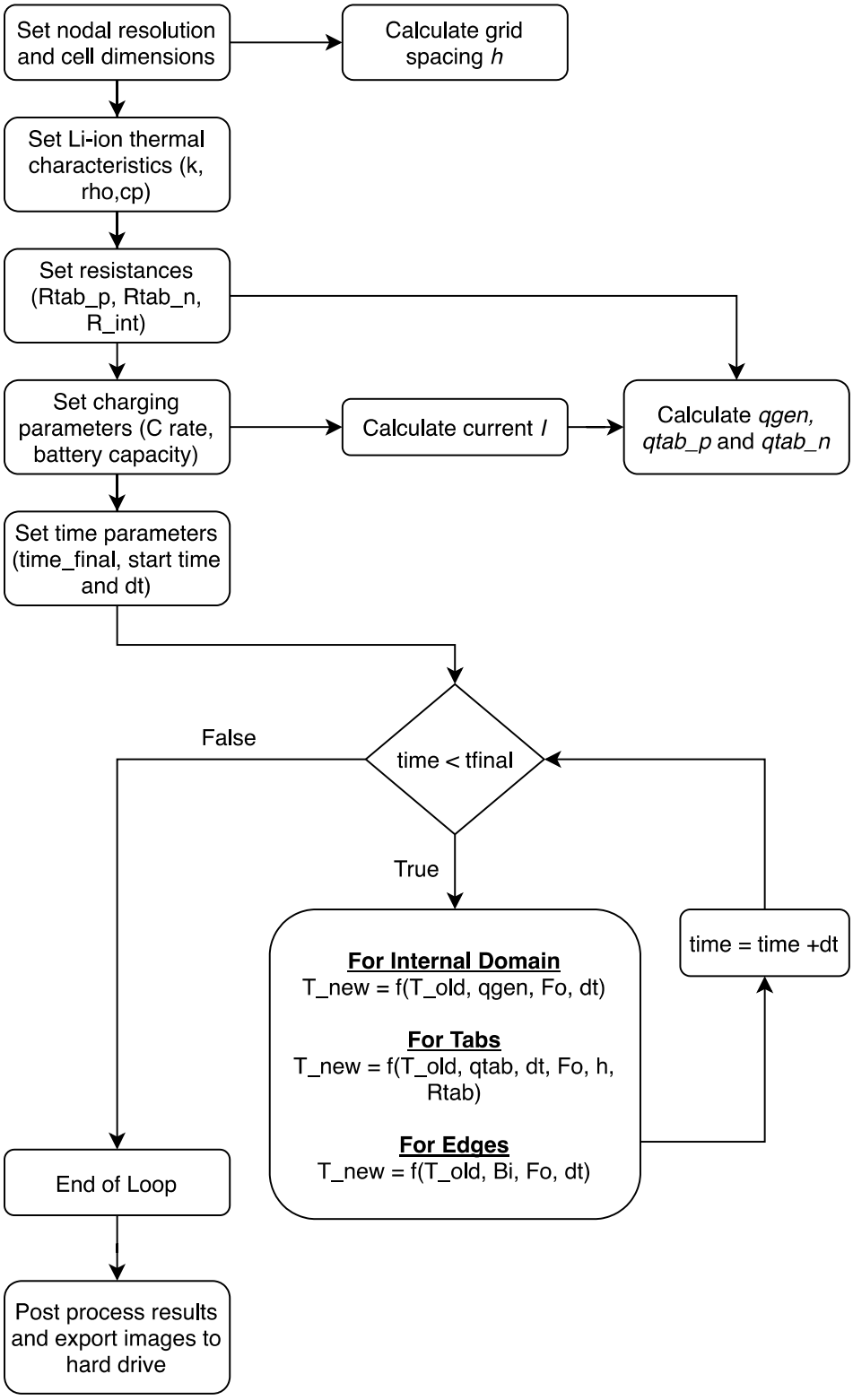

5 Main Work

5.1 Focus of this project

After consideration of the different approaches that could be taken with regards to the project direction, it was decided that the most relevant/suitable direction would be to explore air cooling and phase change material systems as the optimal management systems. This decision was based on the fact that with both systems there are several parameters which can be explored that would aid the battery performance. This will allow the project to investigate multiple input parameters and reach a conclusion as to how the process can be optimized. They offer simple and effective thermal management solutions utilizing natural convection and conduction processes with no need for additional power supply apparatus; this simplifies the design system and reduces the weight of the BTMS. Furthermore, an investigation into these systems will help explore some of the gaps in the available literature, making the project more useful to industrial applications.

Though heat pipes and use of liquid cooling radiators are effective in reducing cell temperature, they introduce added weight and complexity and require energy-consuming parts such as pumps which take away from the power that could otherwise be supplied to the wheels. In place of these systems, the focus will be evaluating the use of PCM and other innovative solutions that are simple and effective. These include options of increasing the thermal conductivity of the cell through the addition of graphene nanoparticles and targeting thermal hotspots with the use of a cooling channel carrying graphene infused mineral oil.

5.2 Early work conducted (Steady State + Dirichlet BCs)

At the start, a simple base code was established as a starting point for the full numerical model to be developed later. The goal was to establish a model that could represent a 2-dimensional lithium-ion battery as a series of nodes which could model temperature distribution in a steady state. At this stage, the code merely solved for the steady state temperature distribution with no internal heat generation term and no heat loss term across the boundaries. Dirichlet boundary conditions were set on all the sides of the battery. The temperature on the right, left and bottom edges are set at an ambient temperature of 20°C and the temperature at the battery tabs is set at 50°C. With this code, there was no ability to

change the discharging rates, heat convection rates, time spent discharging as well as other key parameters of the discharging process and battery characteristics.

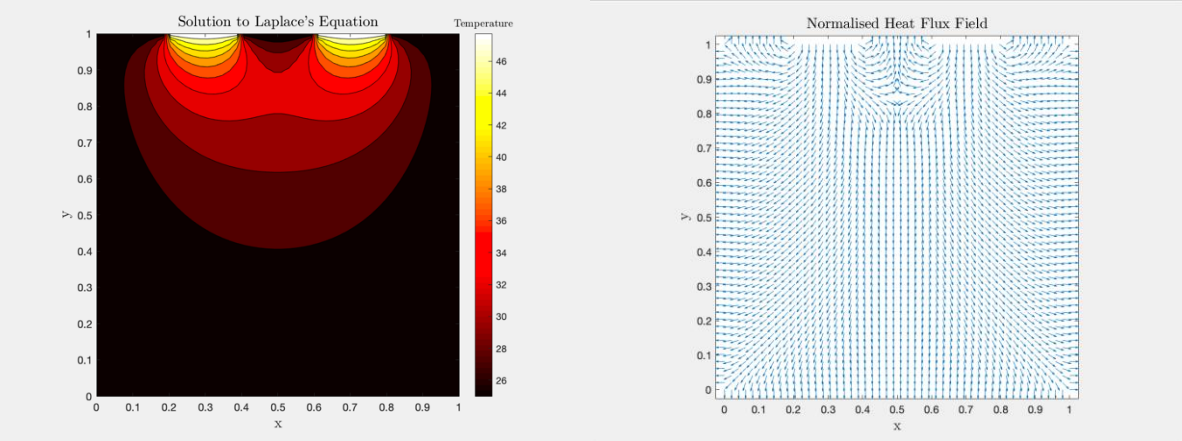

Figure 4 Thermal contour map illustrating temperature distribution and the heat flux field for Stage 1

The results produced matched expectations in terms of the thermal pattern and the magnitude of the temperatures involved.

The code was then extended to account for the internal heat generation term and the internal domain nodes were assigned an additional term to account for the temperature increase. The contour in Figure 5 is different from Figure 4 in that there are greater temperatures near the bottom edge of the cell. The corners and edges remained relatively cold, which is an inaccurate representation of the heating process.

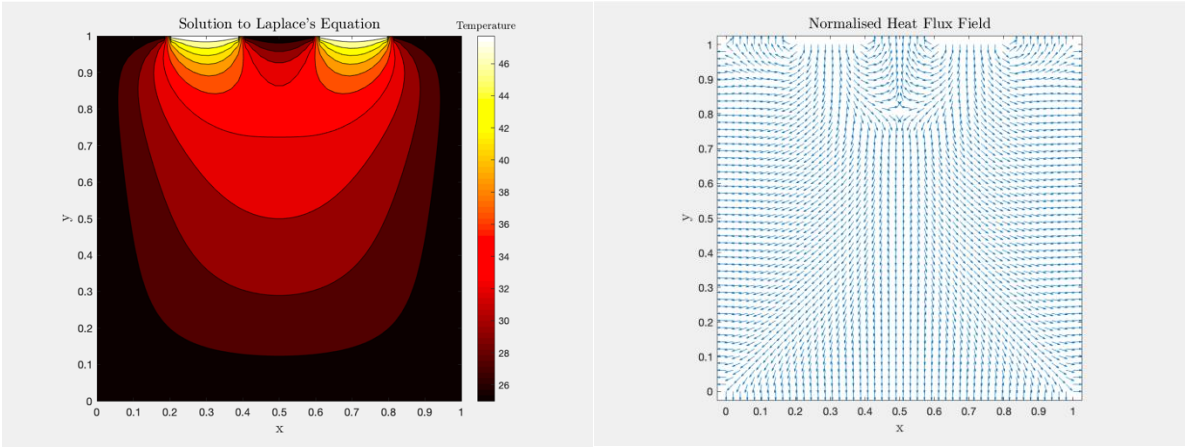

Figure 5 Thermal contour map illustrating temperature distribution and the heat flux field for Stage 2

Overall this early work helped establish a starting point which was to be developed further to make an accurate model representing almost all of the physical parameters that would be found in an experiment.

5.3 Improvements made on the initial code

After the initial code development stage, the following features and changes were added to the code:

1. Ability to march through time using discrete time steps
    a. Heat conduction equations changed to include the $\frac{\partial T}{\partial t}$ terms
2. Ability to change the convection coefficient h to model different cooling rates
    a. Tab boundary conditions changed to Dirichlet boundaries
    b. Side boundary conditions were changed to Robin boundaries
3. Ability to link heat in from the tabs and internal heat generated to current and discharging rate
    a. Current I is now a function of discharging rate and battery capacity
    b. q_{in} from the tabs is now is a function of $I^2 R_{tab}$
    c. q_{gen} is now a function of $I^2 R_{internal}$
4. More accurate representation of the battery thermal characteristics and the antisymmetric properties
    a. Positive and Negative tab resistances were used from literature
    b. Tab widths increased to match measured values from the literature
5. Improved postprocessing of results
    a. Code can now plot Temperature vs Time graphs at selected sensor positions
    b. Colourmap changed to match the results from (Hosseinzadeh et al., 2018).

5.4 Battery Cell Characteristics

Table 3 contains the constant parameters used for the simulation of the XALT Energy® 53Ah NMC pouch. These values are taken from a paper conducted on the characterisation of large-format automotive lithium-ion pouch cells (Kellner et al., 2018), which investigated the same battery cell as the thermal images captured by (Hosseinzadeh et al., 2018).

Table 3 Battery thermal characteristic and parameters

NOTATION	VALUE	DESCRIPTION
$\boldsymbol{k}$	$28\frac{W}{mK}$	Thermal conductivity

$\boldsymbol{c_p}$	$1100\,\frac{J}{kgK}$	Specific heat capacity
$\boldsymbol{\rho}$	$2551.7\,\frac{kg}{m^3}$	Density

The following values were used to model the tabs and the battery's electric and thermal properties (Kellner et al., 2018).

Table 4 XALT Energy® 53Ah NMC pouch cell thermophysical and electric properties

NOTATION	VALUE	DESCRIPTION
$\boldsymbol{R}$	$1.33 \times 10^{-3}\ \Omega$	Resistance of Cell
$\boldsymbol{R_{pos}}$	$3.37 \times 10^{-5}\ \Omega$	Resistance of positive tab
$\boldsymbol{R_{neg}}$	$3.48 \times 10^{-5}\ \Omega$	Resistance of negative tab
$\boldsymbol{W_{pos}}$	$0.08\ m$	Width of positive tab
$\boldsymbol{W_{neg}}$	$0.08\ m$	Width of negative tab
$\boldsymbol{k_{pos}}$	$387\,\frac{W}{mK}$	Thermal conductivity positive tab
$\boldsymbol{k_{neg}}$	$387\,\frac{W}{mK}$	Thermal conductivity negative tab
$\boldsymbol{Bat\ Cap}$	$53\ Ah$	Battery capacity
$\boldsymbol{C\ rate}$	$5\ or\ 3\ C$	Discharging rate

* Tab thermal conductivities were not stated for the XALT battery cell so they were approximated using several references including (Maleki et al., 1999).

5.5 Mesh Convergence Check

It is important to ensure that the solution is independent of the grid used. To check for mesh-independence, the grid resolution was set to a coarse resolution , and the model was solved. Then the mesh resolution was increased slightly, and the new solution is compared with that of the previous coarser grid. If the solution differs then it is not grid independent and the grid is refined further, the model is solved again, and the solution compared again. This is repeated until further refinements in the grid yield no differences in the solution. At that point, we can ensure that the solution is based on physics and is mesh-independent. It is also important not

to use an excessively fine mesh than needed, such that the computational cost of the calculation process can be minimised. If the resolution is too low the results will not have yet converged to what is deemed accurate (i.e. within 0.2% of the true value). If the resolution is too high, the small increase in accuracy does not justify the computational cost in terms of time. Plotted in Figure 6 is the computational time elapsed for each resolution of nodes.

The resolution used for the results presented in this report is 14,400 nodes (a 120 x 120 grid), as the temperature value is within the accurate range and the computational cost is relatively low. This value was chosen on the slightly less accurate end of the spectrum to save computational cost. This was an issue because in the simulations where the thermal conductivity was increased significantly, the time discretization needed to be very small to keep the simulation stable. This would have lead to elapsed times of over 10-15 minutes per simulation.

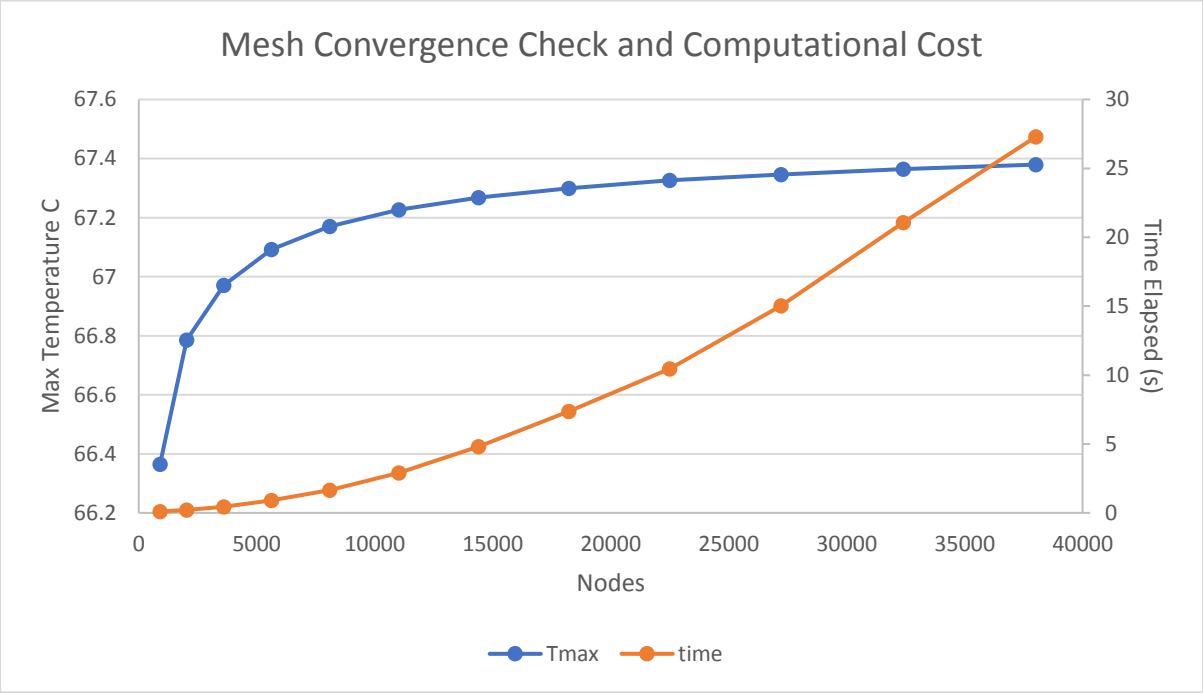

Figure 6 Mesh convergence check plotted to show the trade-off with the computational cost for k=28 W/mK

6 Final Results and Discussion

6.1 Model Validation

To confirm the accuracy of the numerical model and confirm its validity, its results are compared to thermal images created by WMG, University of Warwick (Figure 7). The lab experiment conducted involved discharging the Li-ion battery cell at 3C and 5C discharging rates and capturing thermal images at specified times during the discharge process.

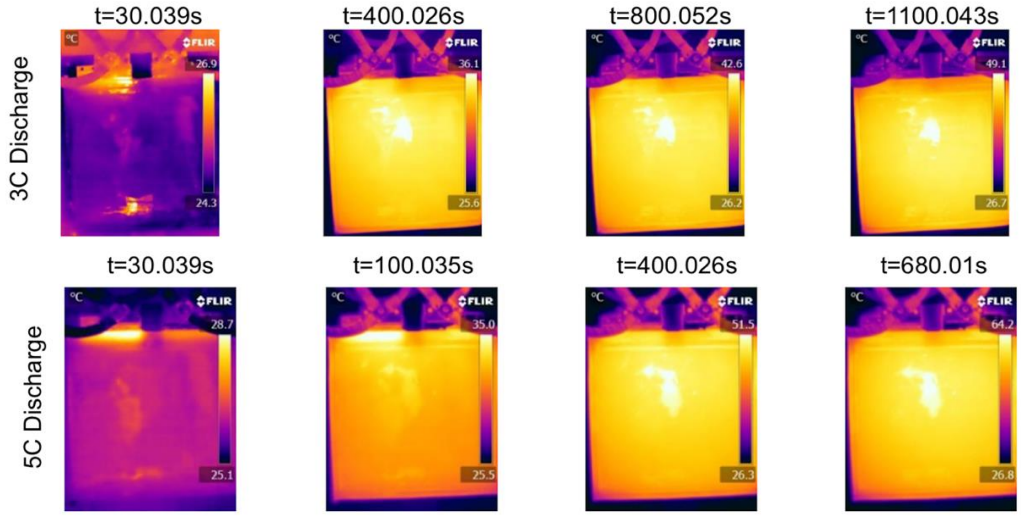

Figure 7 Temperature evolution of 53 Ah cell during a 3C discharge and a 5C discharge rates (Hosseinzadeh et al., 2018)

To replicate these images, the numerical code in Appendix B was run at 3C for 30 seconds, 400 seconds, 800 seconds and 1100 seconds. This was also done for the 5C discharging rate and thermal plots were produced at 30 seconds, 100 seconds, 400 seconds and 680 seconds. For each of the images produced, the colour bar scale is varied to match the corresponding thermal images.

The boundary conditions used in the simulation are chosen to replicate the experimental conditions as closely as possible. In the experiment, the edges of active cell areas are covered by an aluminium casing which helps to reduce the maximum temperatures observed. This means the heat transfer rate from the cell is a result of conduction through the casing as well as natural convection with the surrounding air. To simplify this geometry and model the cell efficiently accounting for conduction/convection, an **effective** heat convection coefficient h was set as 250 W/m^2K. This value was used as it produced results which accurately matched the thermal images from (Hosseinzadeh et al., 2018).

6.2 Validation of results produced under 3C discharging rate with no BTMS

Figure 8 to Figure 11 present a comparison of the temperature contours from the MATLAB simulation and experimental data for 3C discharging after 30, 400, 800, and 1100 seconds.

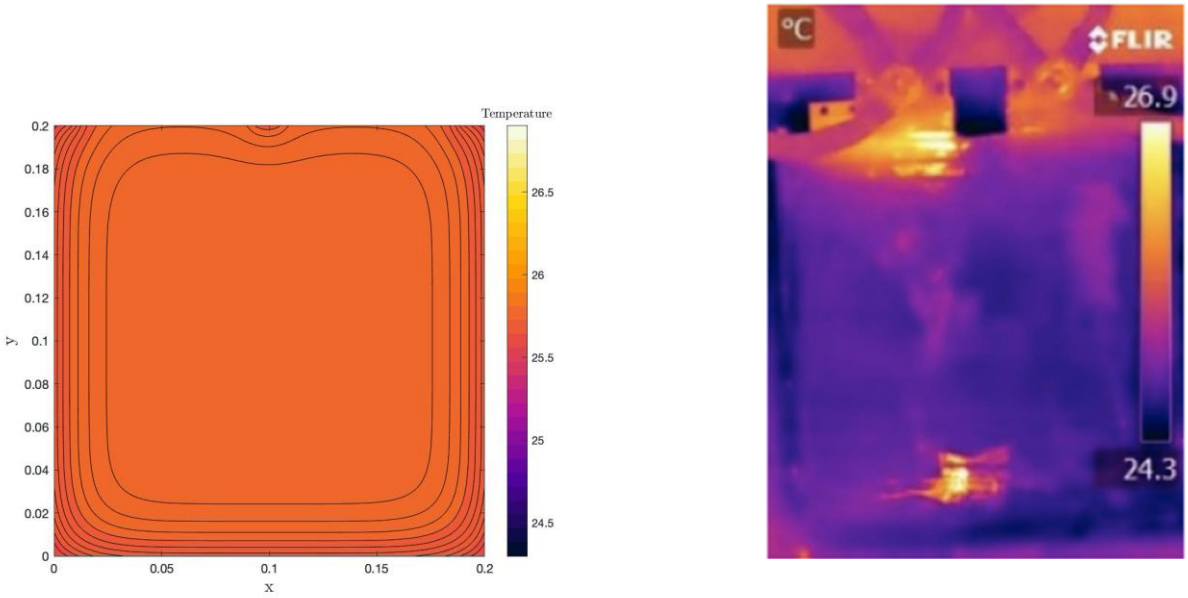

Figure 8 Comparison of experimental results with simulation results for 3C discharging after 30 seconds

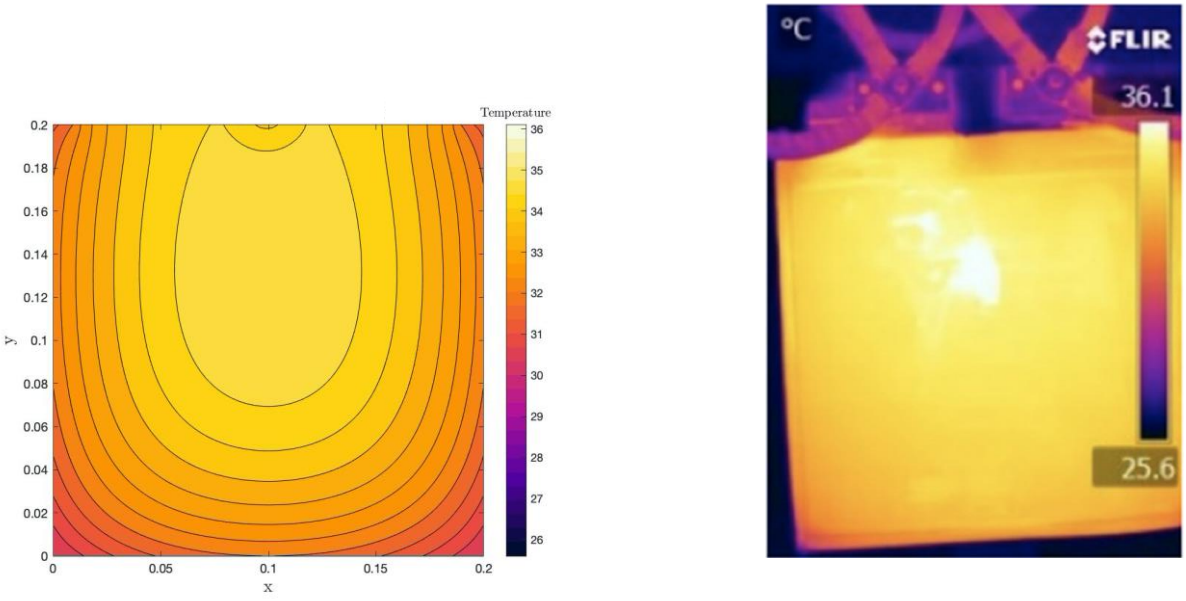

Figure 9 Comparison of experimental results with simulation results for 3C discharging after 400 seconds

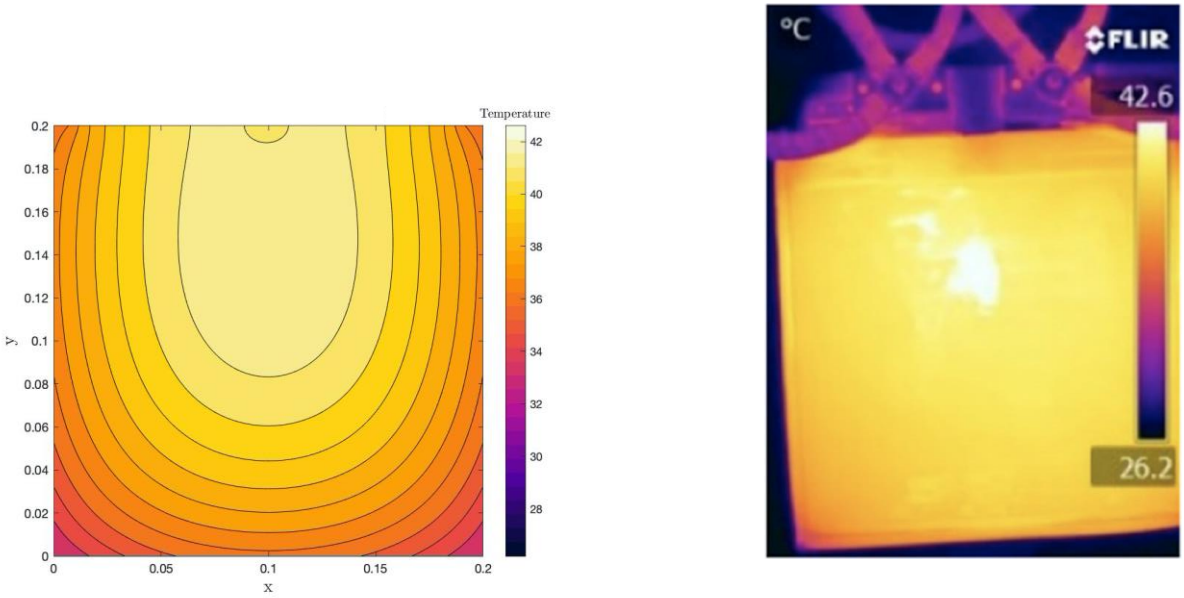

Figure 10 Comparison of experimental results with simulation results for 3C discharging after 800 seconds

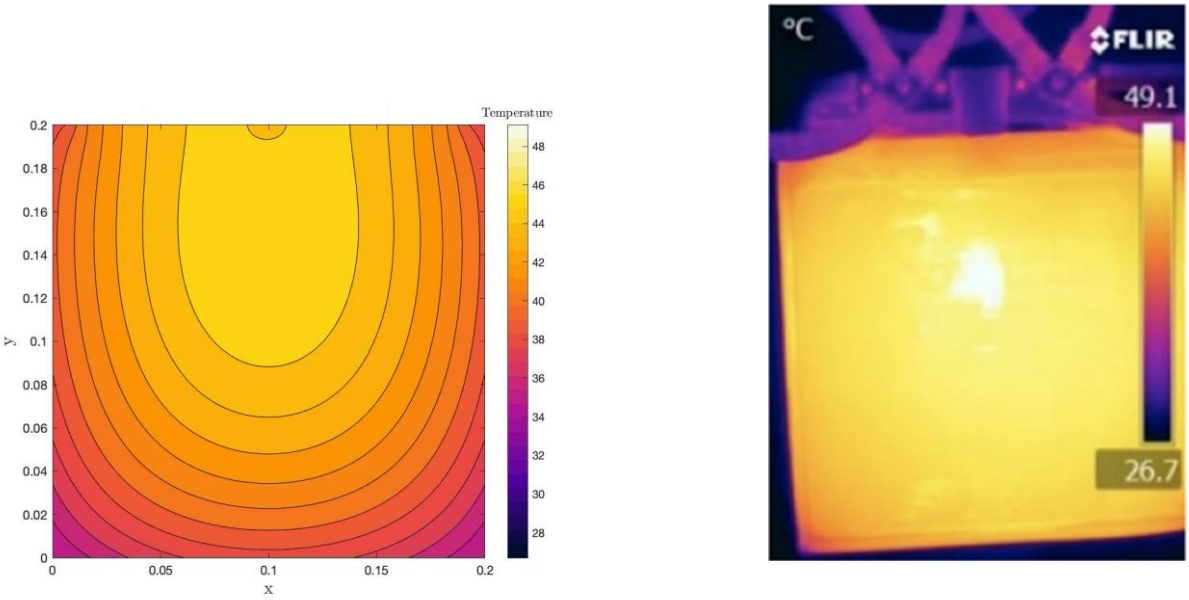

Figure 11 Comparison of experimental results with simulation results for 3C discharging after 1100 seconds

The numerical results compare favourably with experimental findings both in terms of the peak temperature reached and the general trend spatially and in time.

6.2.1 Validation of results produced under 5C discharging rate with no BTMS

Figure 12 to Figure 15 present a comparison of the temperature contours from the MATLAB simulation and experimental data for 5C discharging after 30, 100, 400, and 680 seconds.

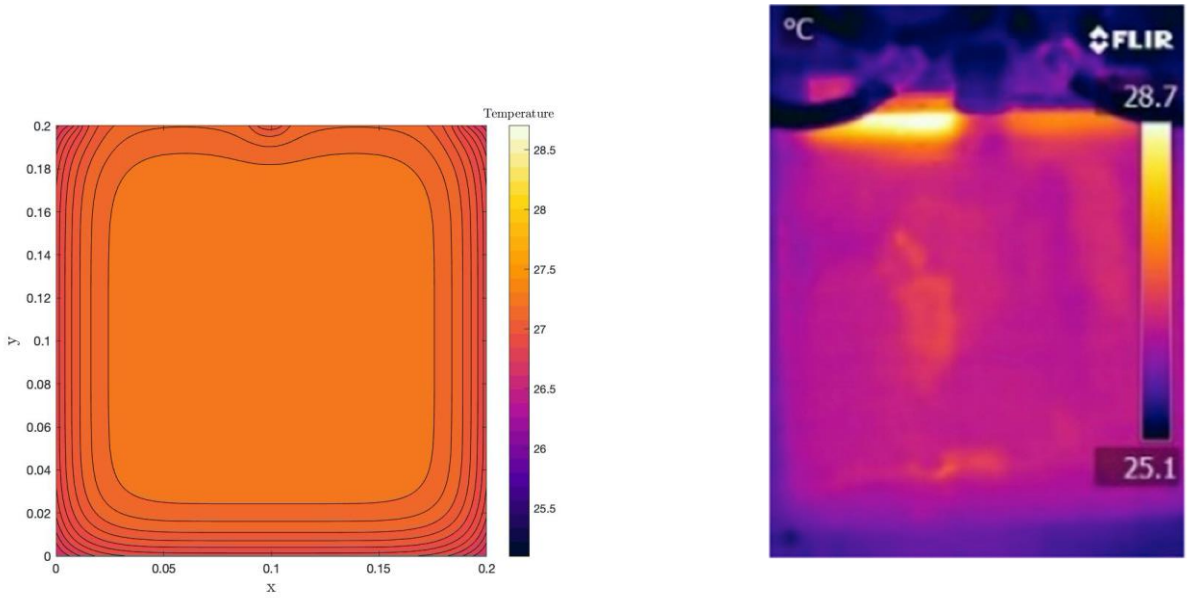

Figure 12 Comparison of experimental results with simulation results for 5C discharging after 30 seconds

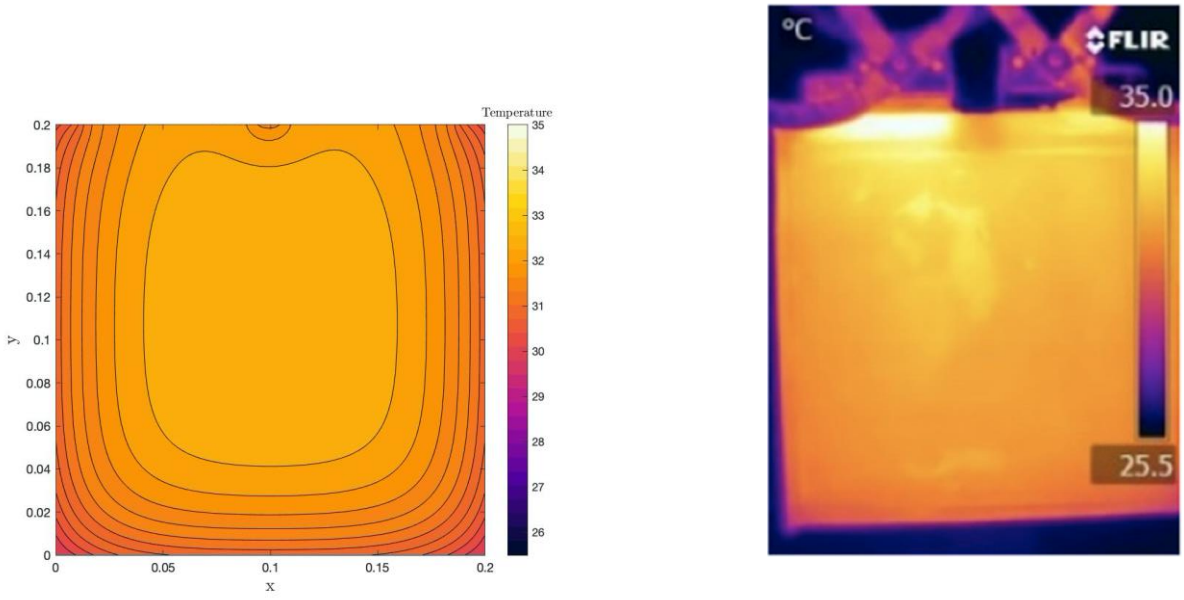

Figure 13 Comparison of experimental results with simulation results for 5C discharging after 100 seconds

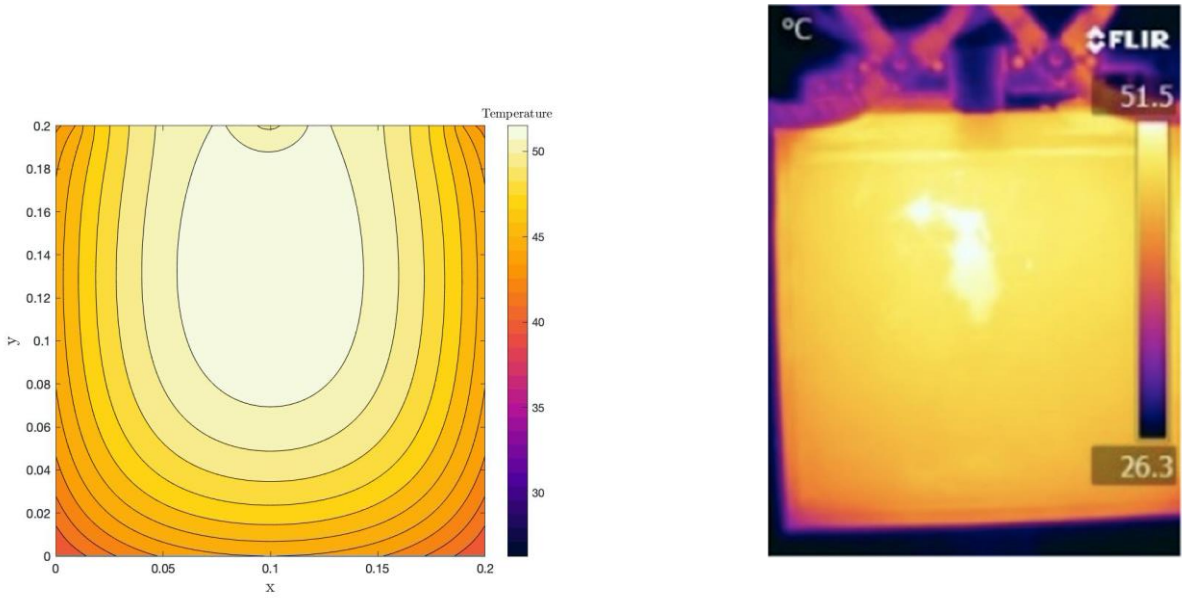

Figure 14 Comparison of experimental results with simulation results for 5C discharging after 400 seconds

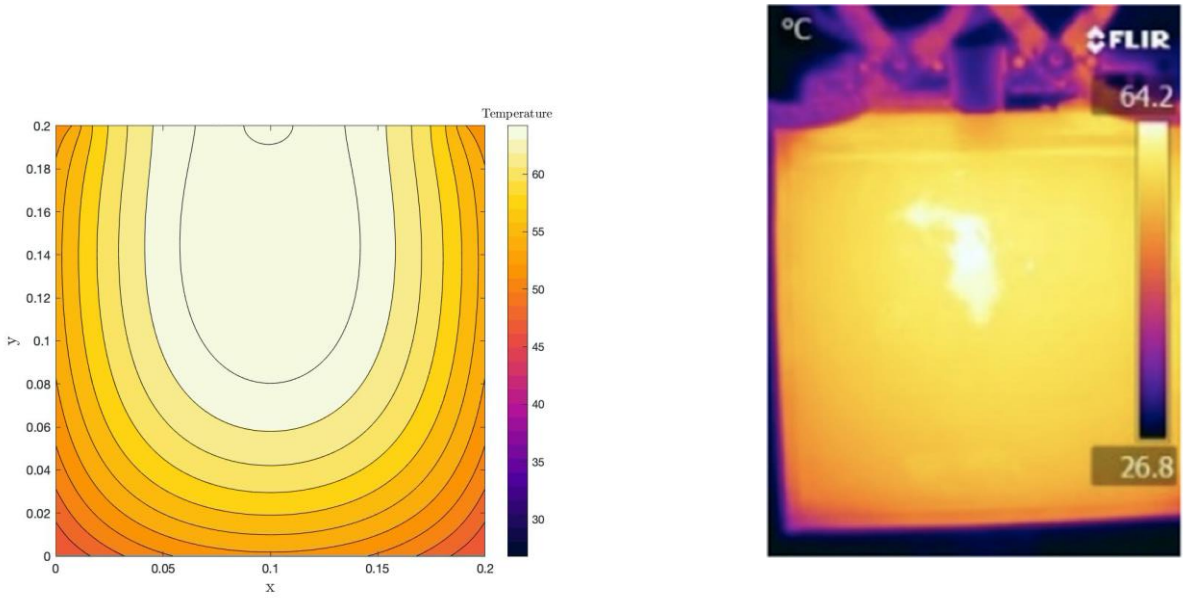

Figure 15 Comparison of experimental results with simulation results for 5C discharging after 680 seconds

Similar to 3C discharge, the model also compares favourably to experiment for the 5C discharge case. The simulation captures the magnitude and location of the peak temperature and is able to predict the trend in time as well.

6.2.2 Model Accuracy

The accuracy of the model was calculated using the following formula:

$$Accuracy = 1 - \left| \frac{T_{max,image} - T_{max,sim}}{T_{max,image}} \right|$$

Table 5 shows the accuracy for each of the 8 cases along with the maximum error and mean error.

Table 5 Model accuracy and validation results

DISCHARGE RATE	TIME	THERMAL IMAGE TMAX	TMAX SIMULATION	ACCURACY
3C	30	26.9	25.82	95.97%
3C	400	36.1	34.98	96.91%
3C	800	42.6	42.06	98.73%
3C	1100	49.1	45.81	93.30%
5C	30	28.7	27.27	95.01%
5C	100	35.0	32.54	92.98%
5C	400	51.5	52.74	97.60%
5C	680	64.2	67.27	95.22%
			Max Error	7.02%
			Avg. Accuracy	95.72%
			SD	2.01%

From the thermal images provided, it is clear that the 5C discharge case needs to be addressed the most, especially the final state of the battery after 680 seconds. With this case, the maximum temperature is 64.2°C which is excessively larger than the 55°C maximum that the literature recommends for safe battery usage. The results produced in this section aim to develop an optimal BTMS that can ensure safe and ideal operation of the Li-ion cell at **all** discharge rates and times. As such, it makes sense to focus on lowering the T_{max} value and lowering the temperature gradients for the 5C discharge case after 680 seconds.

6.3 Case Study 1: Cell thermal conductivity investigation

One of the influential/important cell parameters is the thermal conductivity value (k) for the active cell area domain. The thermal conductivity is a cell's ability to conduct heat, it is a measure of how easily heat can be transferred from one point to another through a given material. The lower the thermal conductivity the less heat can travel and dissipate through

the material, and vice versa. The literature value for the in-plane thermal conductivity for the XALT Energy® 53Ah NMC pouch cell is 28 W/mK. One way of increasing this value is through the addition of graphene nanoparticles to the cell. The numerical model was tested for cell thermal conductivities ranging from 28 – 770 W/mK, the results are shown in Figure 16, Figure 17 and Figure 18.

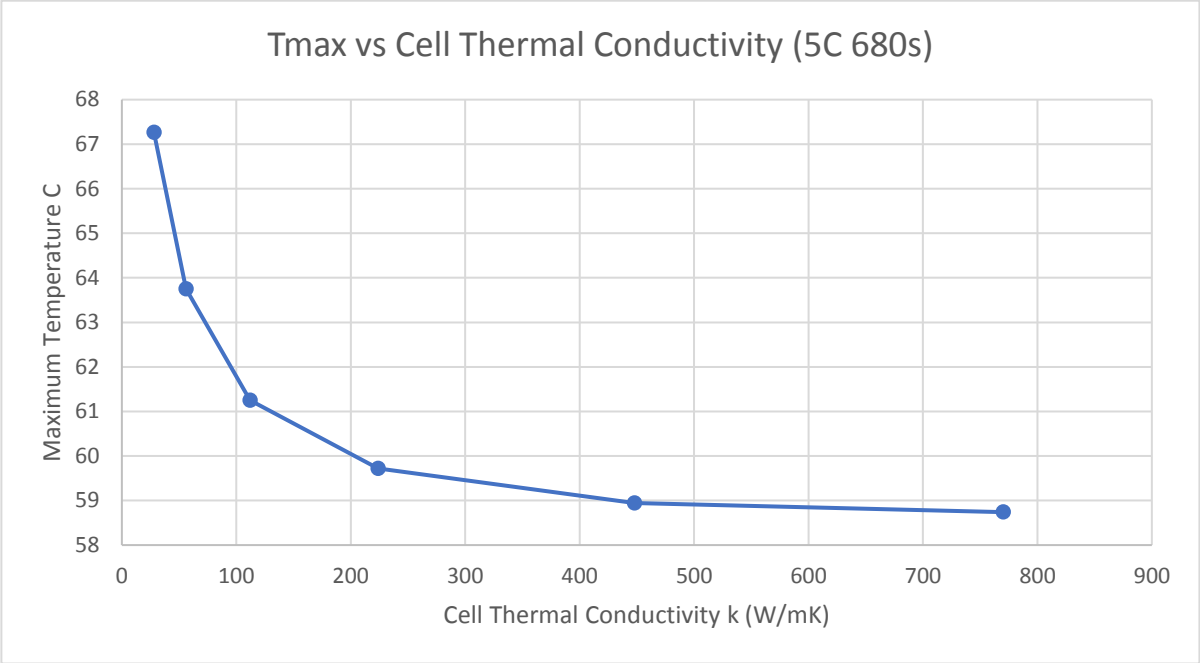

Figure 16 Variation of maximum cell temperature with the thermal conductivity of the cell

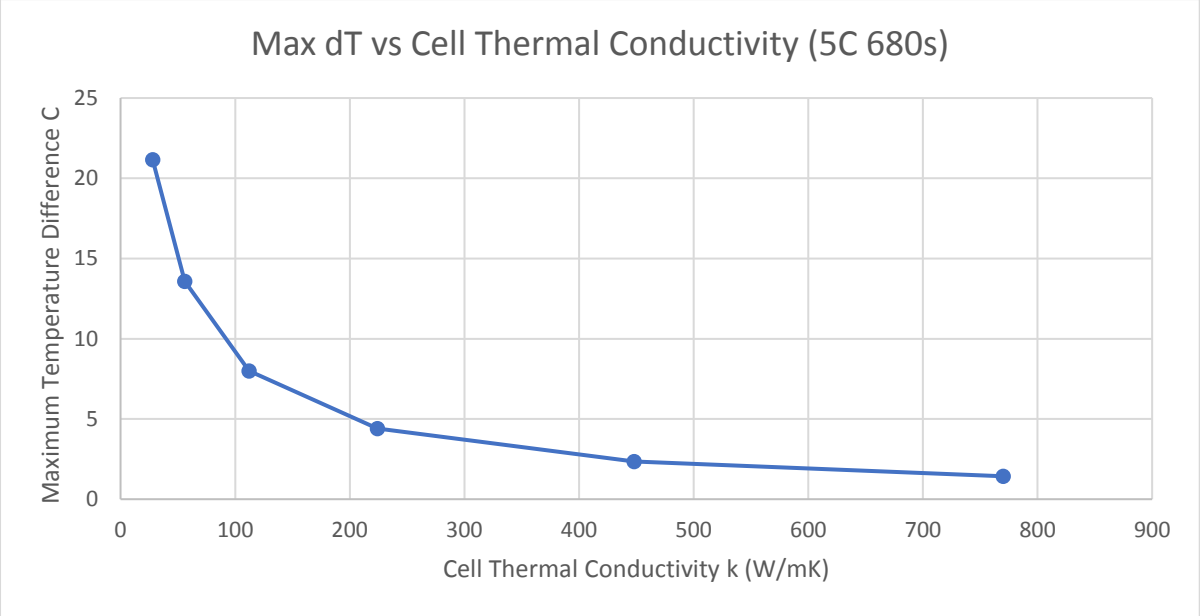

Figure 17 Maximum temperature difference on cell surface under 5C discharge h=250W/m²K

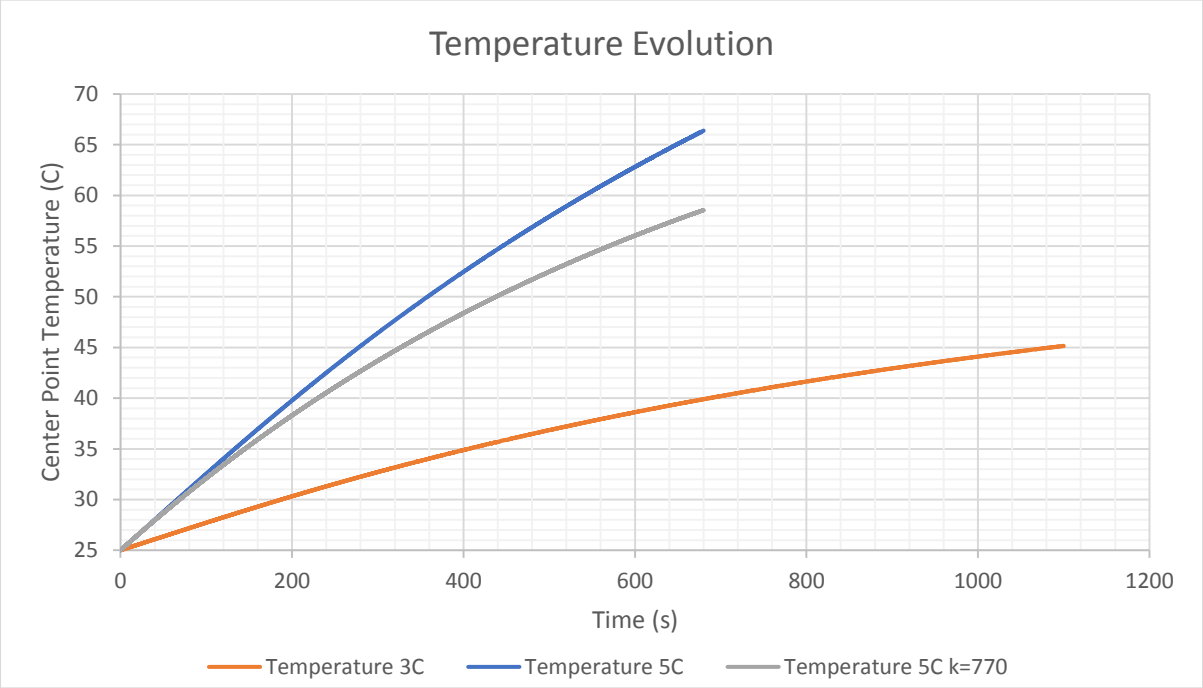

Figure 18 Temperature evolution for the cell under the condition h=250 W/m²K

6.3.1 Evaluation of cell thermal conductivity effects

Figure 16 shows that increasing the graphene composition of the lithium-ion battery cell can lead to significant decreases in the maximum temperature observed on the surface of the cell. By simply doubling the thermal conductivity of the cell, the maximum temperature drops by approximately 3.5°C. There is however a diminishing benefit from increasing the graphene content to very high values. After the thermal conductivity of the cell reaches approximately 300 W/mK, the maximum temperature drops become relatively small.

Figure 17 illustrates the advantage of increasing the graphene content in the battery cell, on the maximum temperature difference measured. As discussed in the Current Context of Project, Li-ion cells are best suited to operating conditions were the temperature gradient does not exceed 5°C. Figure 17 also shows that for all cell thermal conductivities greater than 200 W/mK, the maximum temperature difference will be within the 5°C recommendation.

Figure 18 illustrates the transient effect of the cell thermal conductivity on the temperature evolution at the centre of the battery cell. The final temperature for the 5C case where k=770 W/mK is cooler compared to the original k=25 W/mK cell (58.55°C vs 66.39°C). In practice,

this means that the battery cell can discharge for longer periods while staying within the safe temperature range. The plot for 3C discharge of a cell with k=770 W/mK is not plotted because of the high computational cost of simulating such a long period with a very large α. Furthermore, the 5C discharge case is the limiting condition because of the steep temperature rise and high peak temperatures.

6.4 Case Study 2: Submersion of cell in Phase Change Material

The second investigation conducted looks at the effect of submerging the lithium-ion cell in a phase change material BTSM, as shown in Figure 19, then examining the effect the PCM thermal conductivity has on the cell. The numerical model was tested for PCM thermal conductivities ranging from 0 to 25 W/mK to capture the full effect of the paraffin-graphene hybrids discussed in the Phase Change Material section of the literature review.

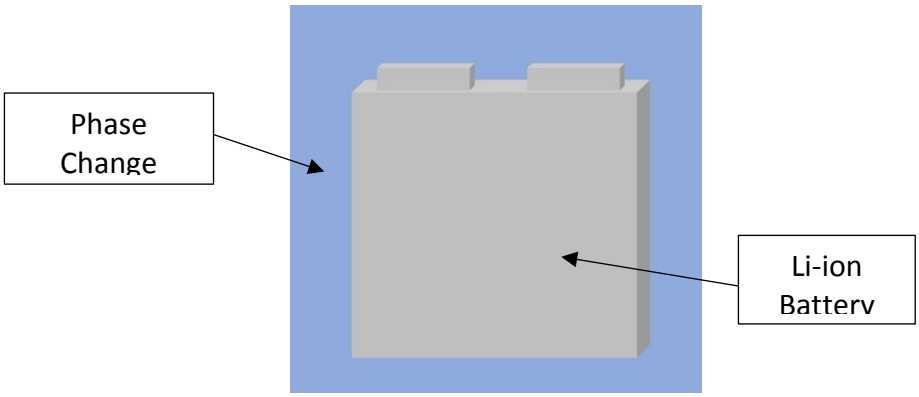

Figure 19 Illustration of the phase change submersion setup modelled in Case Study 2

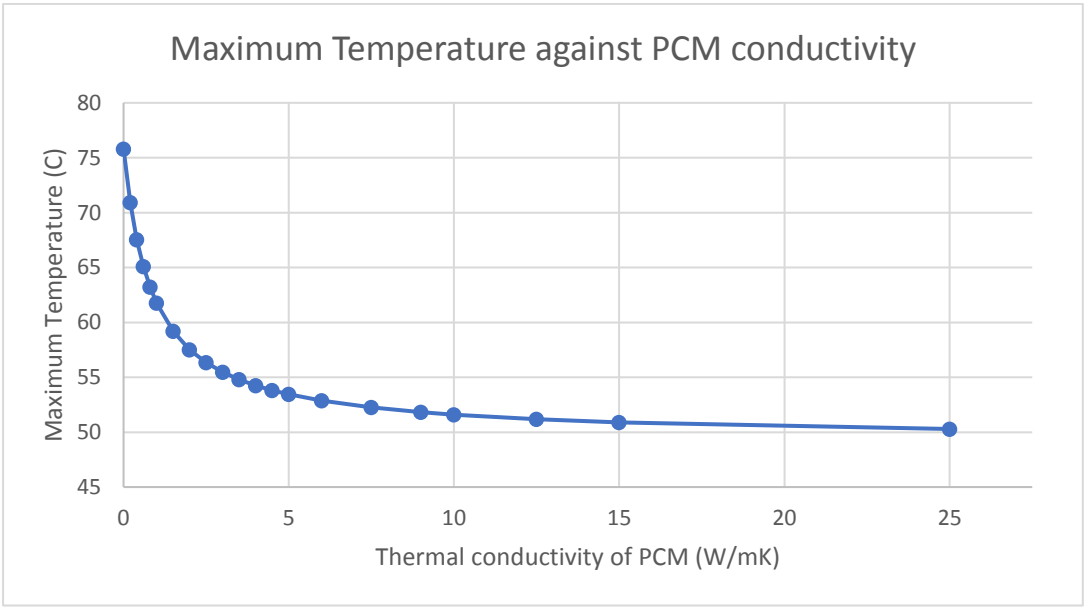

Figure 20 Variation of the maximum cell temperature with phase change material thermal conductivity (5C 680 seconds)

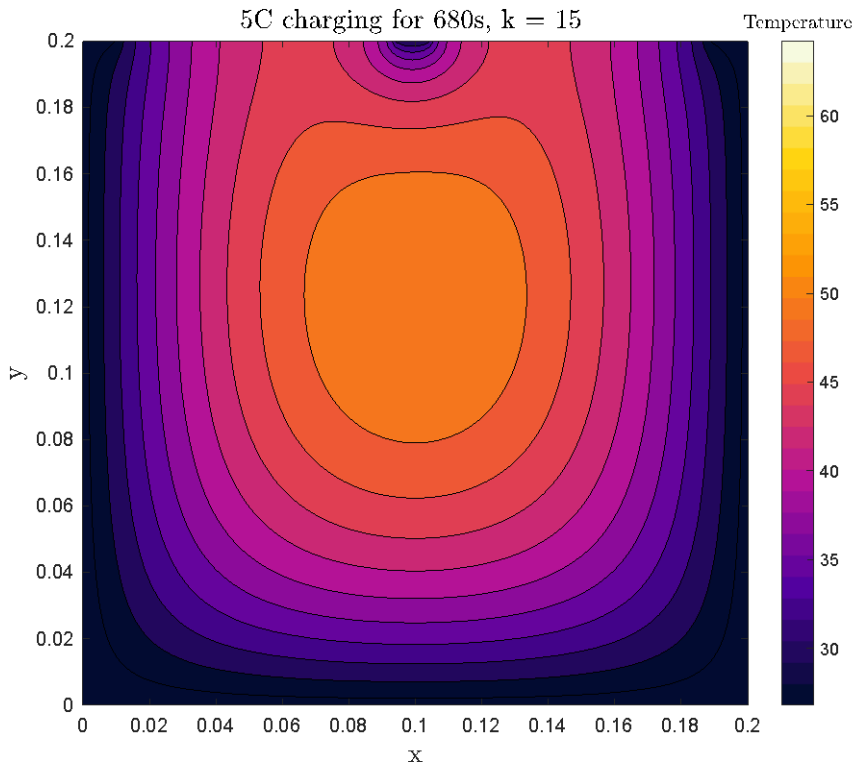

Figure 21 Thermal pattern of cell submerged in a PCM with k = 15 W/mK

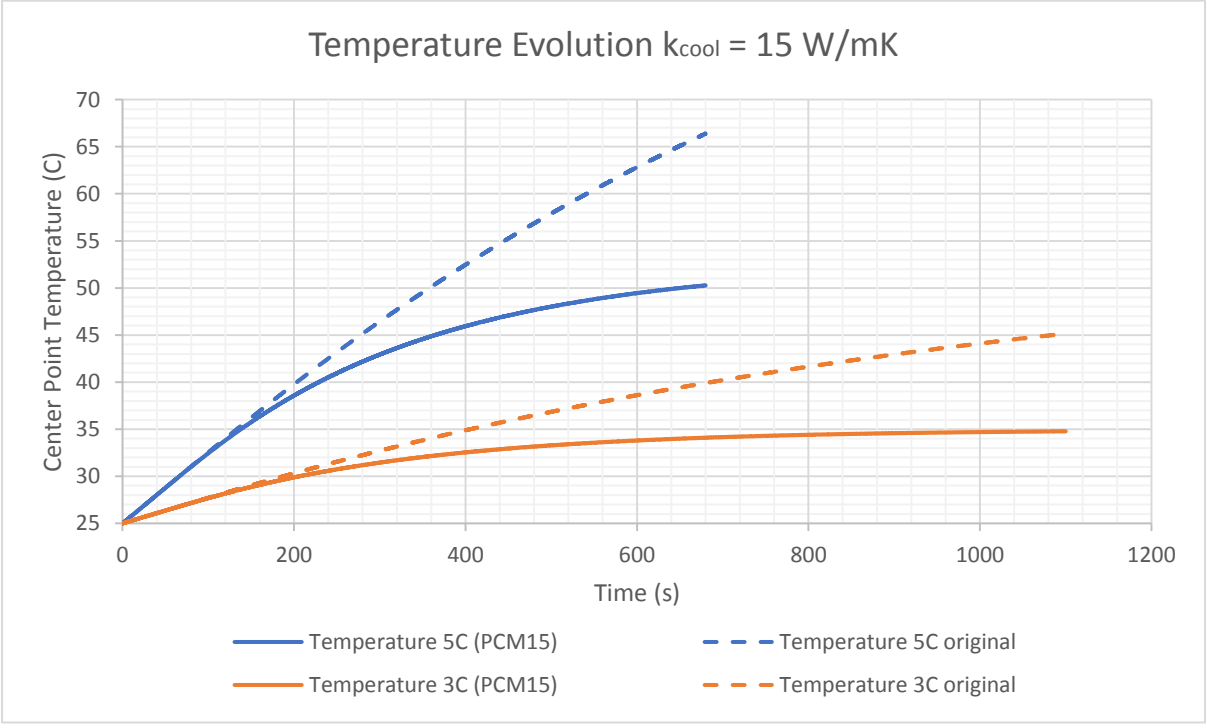

Figure 22 Effect of Phase Change Material submersion on the temperature evolution observed

6.4.1 Evaluation of Phase Change Material Submersion

Figure 20 illustrates the asymptotic relationship between the thermal conductivity of phase change material and the maximum temperature of the cell. Initially, as the thermal conductivity of the PCM increases, large drops are observed in the maximum temperature value. However, after the PCM thermal conductivity reaches a value of 7.5 W/mK, the decreases in T_{max} become minor. From the data collected, it appears that a relatively high graphene content would have to be added to the paraffin hybrid to push the T_{max} value much lower than 50°C. Using Figure 20, it was decided that the optimal thermal conductivity to use for the PCM is 15 W/mK, the equivalent of adding 1 wt.% of graphene nanoparticles. This value also helps to avoid the issue mentioned in the literature of the external shell of the battery heat up too much.

Figure 21 depicts the thermal pattern captured when the battery cell is placed in a PCM of thermal conductivity equal to 15 W/mK. The image shows that although the temperature decreases at all the nodes, the nodes most effected are the side boundaries which cool significantly. However, there remains a hot spot at the centre of the cell which can be expected because the centre of the cell is furthest from the PCM, so it takes the longest time for heat produced to be conducted out to the BTMS. Also, the general centralized nature of the internal heat generation means that the centre will remain hotter for longer.

Finally, Figure 22 shows how the addition of the PCM thermal management system has altered the temperature evolution of the centre of the cell for both 5C and 3C discharge rates. The final temperature of the 5C discharge after 680 seconds dropped from 66.39°C to 50.27°C, a change of $\Delta T = 16.12°\mathrm{C}$. The plot also shows improvement for long-run 5C discharges when the PCM is installed, the temperature will likely asymptote to a value of 55°C, ensuring optimal/safe discharge for a longer time. Similarly, the 3C discharge has been improved and the temperature at the centre of the cell appears to asymptote to 35°C.

6.5 Case Study 3: Internal cooling channel effect

The final case study looks at installing a cooling channel through the hotspot identified in the previous case studies. It was hypothesized that if the hotspot temperature was addressed,

then the average temperature would decrease significantly. The channel is designed to have length and height 0.08m, but in order for the battery to include the same active material as the original case, the length and width of the battery cell were increased to 0.2154m. Figure 23 shows what this cooling channel would physically look like. A 24-node x 24-node channel was cantered at the nodal position (i=60, j=76) to model this.

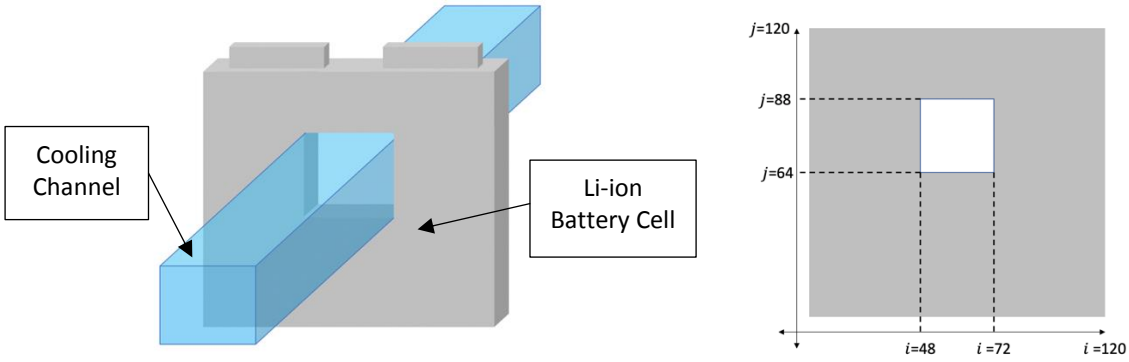

Figure 23 Illustration of the cooling channel setup modelled in Case Study 3 and the position of the channel

The cooling fluid used inside the channel was set as mineral oil with C_{60} fullerene nanoparticles. Table 6 contains the thermofluidic values used for the coolant, these values were captured at a temperature of 25°C (Dombek et al., 2018).

Table 6 Thermofluidic properties of mineral oil with C60 fullerene nanoparticles

THERMOFLUIDIC PROPERTY	VALUE
Thermal conductivity	$0.133\,\frac{W}{mK}$
Specific heat capacity	$1945\,\frac{J}{kgK}$
Density	$867\,\frac{kg}{m^3}$

The boundary conditions within the channel were set as Neumann boundary conditions, with the heat transfer being through conduction only. The temperature of the coolant is initially set to 25°C, however, this value changes over time as it is heated by the cell.

6.5.1 Results for Cooling Channel + Natural Convection

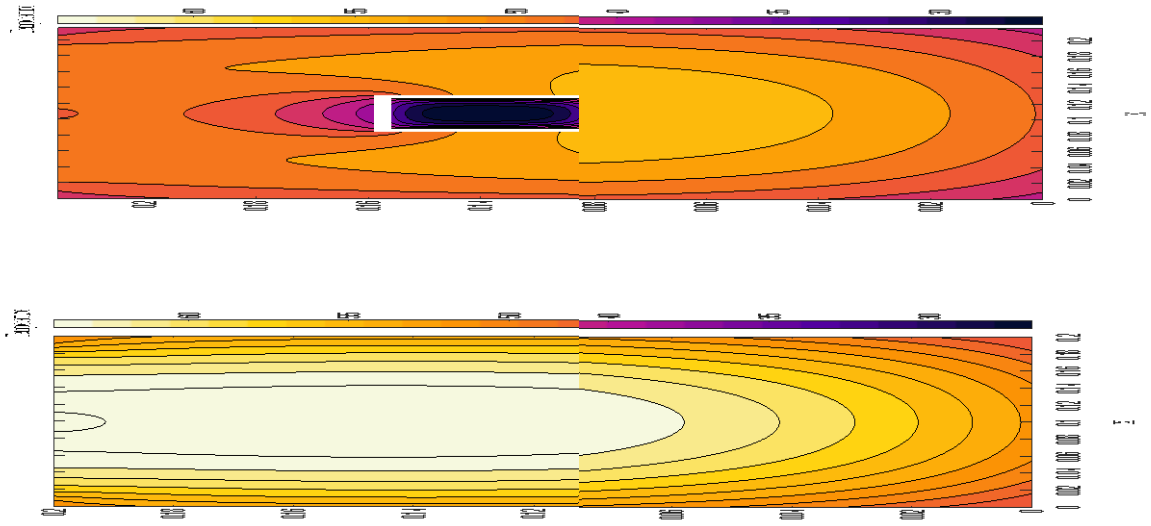

Figure 24 Comparison of with channel and without channel under external natural convection of h=250W/m²K

	Normal Cell	Cooling channel installed
Max Temperature (°C)	67.27	58.42

Figure 24 depicts the effectiveness of the cooling channel as a thermal management system, and how it addresses the issue of a central hotspot within the cell. Firstly, the maximum temperature measured drops by 8.85°C a significant improvement on the normal operating conditions. Furthermore, the average cell temperature drops significantly to around 50°C, which is within the safe operating range for lithium-ion cells. Also depicted is the decrease in the temperature difference between the sides and the centre, which as discussed in the literature review can improve long-term performance and battery life. The presence of the cooling channel slightly near to the top of the cell also helped to cool the tabs. In the original cell, the tabs would heat up to almost 70°C, whereas with the cooling channel installed they are around 50°C.

6.5.2 Results for Cooling Channel + PCM submersion

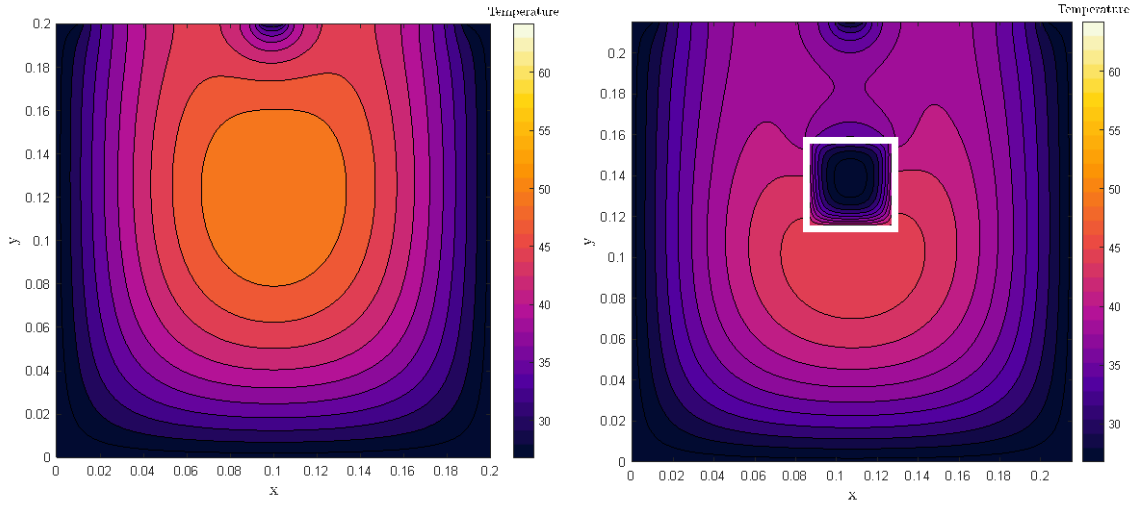

Figure 25 Comparison of with channel and without channel under external phase change material of k=15 W/mK

	Normal Cell	Cooling channel installed
Max Temperature (°C)	50.90	46.37

The submersion of the battery cell in high conductivity PCM, with a cooling channel installed, is illustrated in Figure 25. The effect of the cooling channel on the thermal pattern is very similar to the effects depicted in Figure 24. The position of the thermal hotspot is pushed down, to below the channel, and the maximum temperature within the cell decreases by 4.53°C. This smaller change in T_{max} of the cell compared to the natural convection case can be explained by the smaller temperature difference between the cell temperature and coolant temperature seen in the no-channel case using PCM, Figure 21. Because the temperature difference between the cell and the 25°C coolant is small, the heat transfer rates observed are low, as governed by Fourier's Law.

7 Conclusions

This project aimed to investigate the effectiveness of different thermal management systems, and to compare their performances to find an optimal solution for an electric vehicle application. To come to a decision on the optimal BTMS, a numerical model was developed to represent the Li-ion battery in 2 dimensions. The model was validated using experimental data. The primary objective was to find an optimal operating setup which reduces the maximum temperature and temperature gradients while also allowing for a high-power output.

7.1 Case study conclusions

A comparative study is presented in Figure 26 and Figure 27, to illustrate the effect that each thermal management approach can have on the maximum temperature and how the combination of BTM systems can improve cooling power. To evaluate each of the thermal management system configurations mentioned in this report, the results are measured against a set standard/base case.

For Figure 26, the first bar represents the base case, where no thermal management system is installed, and the heat loss is through natural convection only.

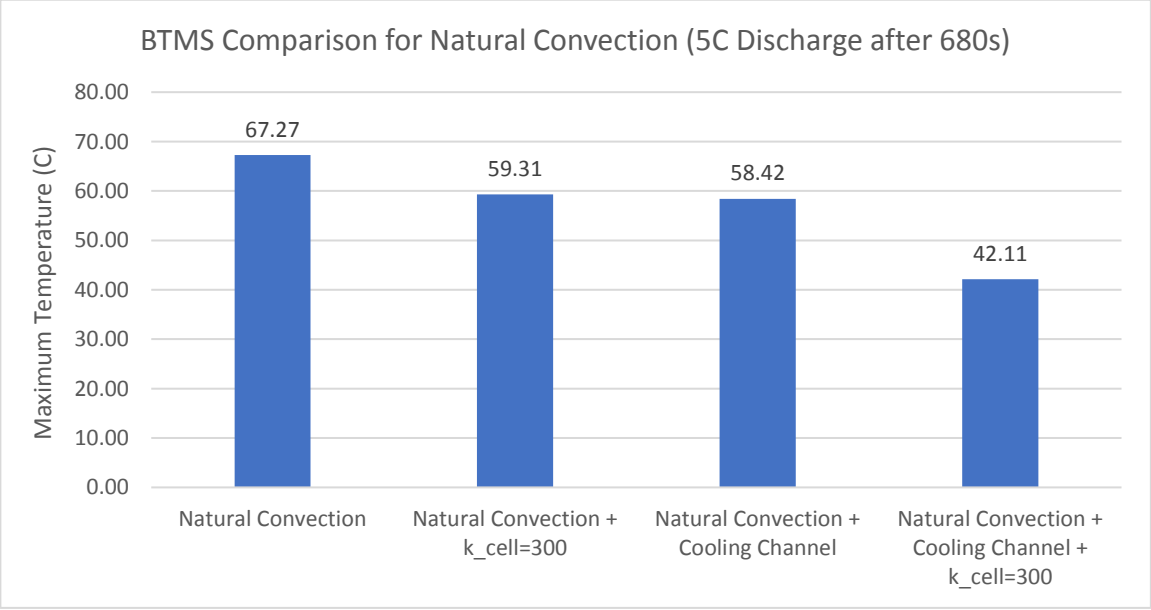

Figure 26 Comparative study showing the effect of installing BTM systems on a cell in the natural convection case

Firstly, the enhancement of the cell's thermal conductivity to $k_{cell} = 300$ W/mK, through the addition of graphene nanoparticles within the cell, drops the maximum temperature by 8°C, a 12% decrease in temperature compared to the base case. Secondly, the addition of a cooling channel, containing mineral oil infused with C_{60} fullerene nanoparticles, through the cell drops T_{max} by 9°C, a 13% decrease from the base case. Thirdly, a combination of enhanced cell conductivity and a cooling channel addition cause the maximum cell temperature to decrease by 25°C, a 37% decrease from the base case.

For Figure 27, the first bar represents the base case, where the cell is submerged in a PCM thermal management system.

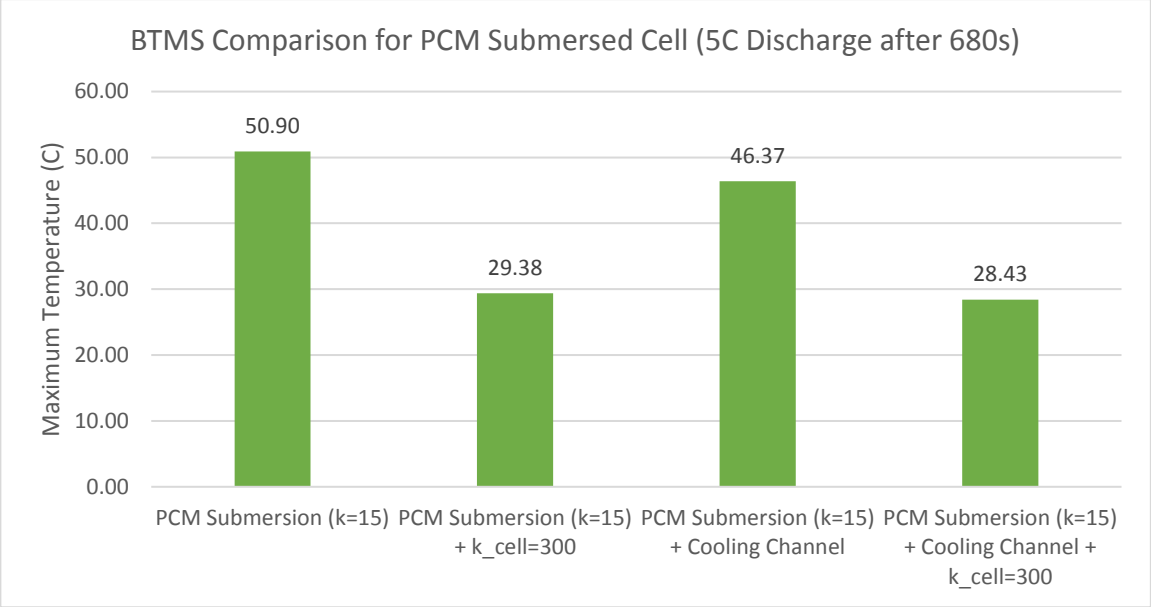

Figure 27 Comparative study showing the effect of installing BTM systems to a PCM submersed cell

Figure 27 illustrates the effect that the same thermal management methods used in Figure 26 can have when the cell is instead submerged in a PCM ($k_{PCM} = 15$ W/mK) as opposed to just using natural convection. The phase change material used in the comparison was selected using the discussion presented in the Evaluation of Phase Change Material Submersion section. Firstly, the enhancement of the cell thermal conductivity drops the maximum temperature of the cell by 21.5°C, which correlates to a 42% decrease from the base case. Secondly, the installation of the cooling channel to the already submerged cell leads to a drop of only 4.5°C, the equivalent of a 9% drop. Finally, the combination of both the cooling channel and the enhanced cell thermal conductivity to the already submerged cell, drop T_{max} by 22.5°C, which equates to a 44% decrease from the base case.

7.2 Optimal BTMS solution

It is the opinion of this report that the ideal thermal management system for lithium-ion battery cells is the use of graphene nanoparticles to enhance the cell thermal conductivity to 300 W/mK and submerging this cell in phase change material of thermal conductivity 15 W/mK (see Figure 27 bar 2).

This conclusion was decided through the following process of elimination. Firstly, all combinations of thermal management systems which included natural convection for the external cell wall were eliminated (Figure 26 all bars eliminated). This is because the use of a phase change material surrounding significantly dropped the maximum temperature when applied to any combination of BTM systems. Then the PCM submersion only was eliminated because its maximum temperature was still relatively high compared to alternate combinations. The PCM submersion with graphene infused mineral oil cooling channel installed (Figure 27 bar 3) was the next to be eliminated. The remaining combinations were PCM with an enhanced cell and PCM with an enhanced cell and a cooling channel (bars 2 and 4 of Figure 27 respectively).

The decision to choose the slightly higher temperature option represented by bar 2 of Figure 27, as the optimal BTMS was because the temperature shortcoming was merely 0.95°C, but avoided the complexity of installing a cooling channel. It was surprising that adding the cooling channel did not have a larger impact on the temperature drop, however, this can be attested to the small temperature difference between the cell and the channel making heat transfer rates insignificant. The cooling channel was also not included because the slight advantage in maximum temperature would come at the expense of parasitic power being taken from the cell.

Originally, it was assumed that the safest operating conditions for the cell were low discharge rates such as 3C, as these would ensure low operating temperatures for prolonged periods as well as helping to improve battery health. However, with the optimal BTMS installed the 5C discharge rate temperatures are kept low, they asymptote to approximately 29.5°C. As a result, this BTMS achieves the goal set out for this project, to reduce the operating temperature while maximizing power output. The disadvantage, however, of using this BTMS

is the added weight that is associated with the PCM as well as the heating effect the PCM will have on the cell during idling. However, overall this design presents numerous benefits which greatly outweigh its drawbacks, making it ideal for industrial application.

7.3 Limitations of the project

7.3.1 Numerical and analytic nature of the code

The heat equation solver designed was built using an explicit two-dimensional finite difference method. Although this scheme is simple to implement there is a major disadvantage in the processing times involved for long discharging times. This is because of the size of the time discretization term Δt. To keep the simulation stable (i.e. the results produced never exceed physical limits), the Δt must meet the following requirement (Becker and Kaus, 2016):

$$\Delta t \leq \frac{\min((\Delta x)^2, (\Delta y)^2)}{4\alpha}$$

For a grid of 60x60 nodes, the time interval must be less than 0.288s. For simulations with a greater nodal resolution, the computational costs increase exponentially.

7.3.2 Constant internal resistance

Another disadvantage of this method of coding is that it relies on accurate measurement or representation of the physical model as well as a sound knowledge of the chemical and material compositions for an accurate representation (Shabani and Biju, 2015).

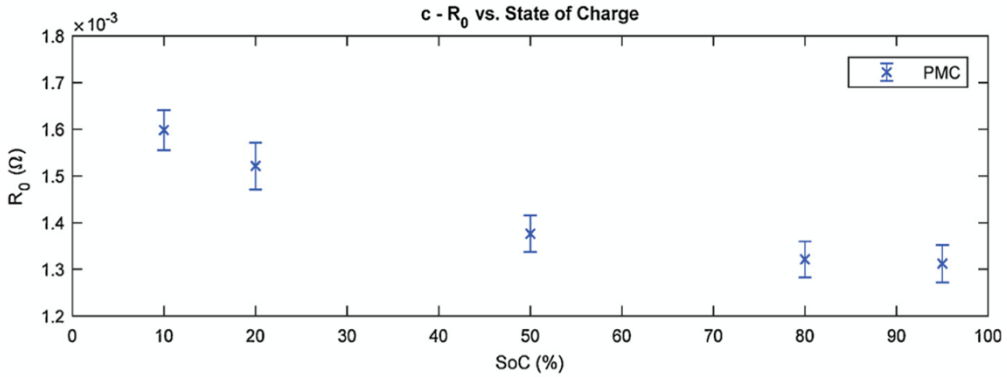

Figure 28 Experimental investigation of internal resistance R against the state of charge (Kellner et al., 2018)

The internal resistance value used in this project was constant, 1.33e-3 Ohms, throughout the entire discharge. This value was stated in the literature given for the XALT Energy® 53Ah NMC pouch cell. However, in reality, the internal resistance is a function of the state of charge of

the cell itself. Figure 28 shows that at the start of the discharge process, the resistance can be as large as 1.6e-3 Ohms (Kellner et al., 2018). However, for the majority of the discharge process, the internal resistance is between 1.3e-3 and 1.4e-3, making the approximation of 1.33e-3 suitable.

7.3.3 Effect of nearby cells

One of the challenges of correctly modelling electric vehicle battery cells is the fact that the nearby cells can often have a great effect on the maximum temperatures achieved within a single cell. Radiation from adjacent cells will increase the temperature of the cell as well as increasing the temperature of the surrounding air. Also, efficiently designing the electrical configuration of the cells can help reduce temperatures, as the current flowing through a single cell can be optimised through the use of a proper circuit.

7.4 Future work

7.4.1 Applying heterogeneous steady thermo-physical properties

An assumption is made that the entirety of the battery cell is homogenously composed of the same thermo-physical properties unless otherwise defined. This, in reality, is not accurate, as the composition of the internals of the battery cell leads to a distortion of this continuity assumption. The cathode and anode as well the separator plates will have different conductivities and each will affect the thermal patterns developed in the cell. Furthermore, the accuracy of this model is hindered by the assumption that the internal properties of the cell remain constant throughout the discharging process. However, in reality, there is a significant relationship between the state of charge of the cell and the physical properties the battery exhibits. For all the parameters set in this code, the values used were taken at 50% state of charge, which is the midpoint of the discharge. As a result, a certain level of accuracy is lost in the process. In the future, it would be beneficial to vary the values set in Table 4, as functions of the state of charge. Several research projects have investigated this and have developed formulae approximating voltage, thermal conductivity, and entropy change as functions of the state of charge.

7.4.2 Simulating entire load cycles

The next step in developing the code is to model an entire loading cycle of the battery cell to investigate the effect of one typical loading cycle on the temperature of the cell. To do this

the heat generation terms will be a function of time, matching the testing schedule illustrated in Figure 29, which is adapted from research done by the University of Waterloo (Chen, 2013). Heat is generated by the battery during the charging section (80-120mins) and the temperature continues to rise until the resting section starts at the 120-minute mark. During the resting stage, there is time for heat to be transferred away from the battery and the temperature to drop to cooler levels. After that, there is a discharging stage which starts at 250mins until the 540-minute mark. It is expected that the greatest temperature will be at the 120 min mark and the next highest would be at the 540-minute mark after charging is complete.

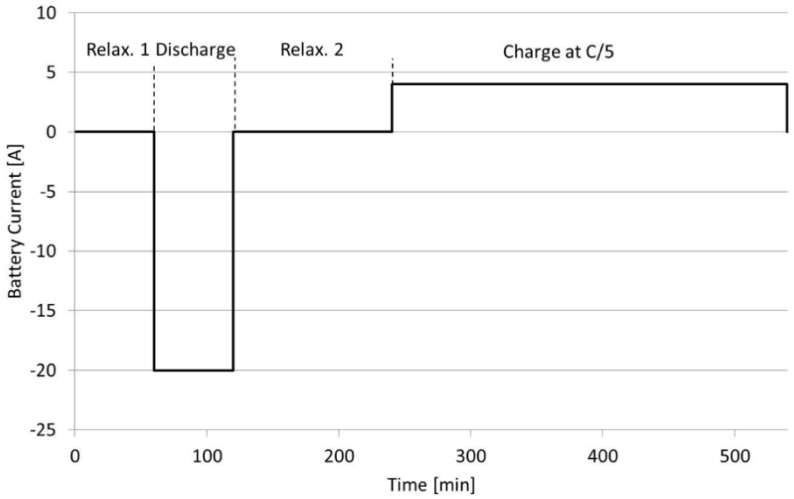

Figure 29 Testing schedules for current(A) for Li-ion battery examination (Chen, 2013)

7.4.3 Simulating battery cell degradation

Another aspect to consider in the future is investigating the degradation of the lithium-ion cells over more cycles. The current model works on the assumption that no degradation occurs as a result of previous loading cycles, which is inaccurate. One way in which the current model can be adjusted is by creating an external database that stores data from previous load cycle simulations and the code then uses that data to calculate potential losses in the capacity of the cell. It is then useful to continue that investigation, to examine the long-term effect of many loading cycles can have on battery performance. This is important to the subject of thermal management systems as battery lifespans can be greatly improved by effectively monitoring and controlling cell temperatures. In reality, electric vehicle batteries can lose up to 40% of their capacity over 5 years. Research conducted at Columbia University indicated

that about 90% of the battery capacity can be saved over 5 years, by simply keeping the cell temperature below 25°C, (Xu et al., 2016), as shown in Figure 30.

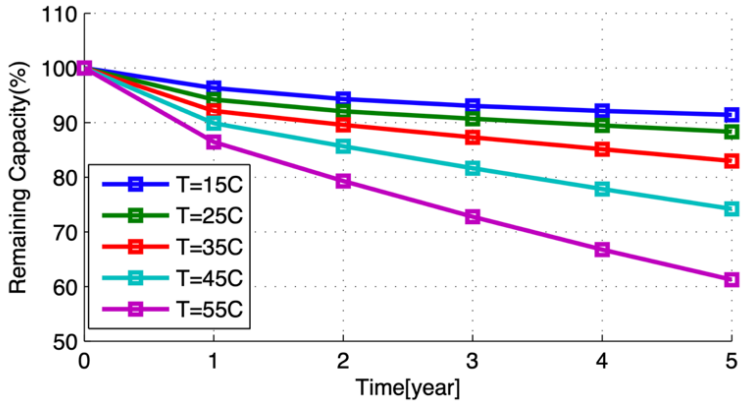

Figure 30 Calendar ageing with varying temperature at 50% SoC (Xu et al., 2016)

7.4.4 Effect of initial cell and ambient temperature

Two main factors that affect the final temperature of a battery cell after a discharge cycle are the initial cell condition/temperature and the ambient air temperature. A lower initial cell temperature will mean a lower average temperature during the initial operating stages, this can help improve battery life and reduce the risk of the thermal runaway. Furthermore, the ambient temperature is the main driving force for convection away from the cell. According to Newton's Law of Cooling, the larger the temperature difference the greater the heat transfer rate, which in turn means the cooler the surface. Also, the initial cell temperature plays an important role in the internal resistance of the cell, at lower temperatures the cell exhibits significantly larger resistance. Shanghai Jiao Tong University investigated this and found that the internal resistance of a cell, at 50% state of charge, can increase by up to 44% when the temperature is dropped from 30C to 0C, as shown in Figure 31 (Ma et al., 2018).

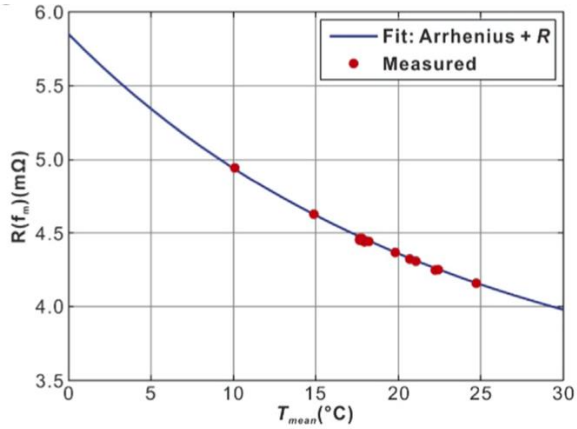

Figure 31 Internal resistance variation with the mean cell temperature for a 30A current pulse

7.5 Success of the numerical code

7.5.1 Flexibility

The main feature of the code developed is the ability to change process parameters easily. Features of the battery cell such as thermal conductivity, density and specific heat capacity can be changed under the Battery and Thermal Characteristics section. This allows the model to be changed for different cell types not only the XALT Energy® 53Ah NMC pouch cell. Modification of the battery's size and physical features is much easier compared to traditional software such as ANSYS, where a new geometry and mesh must be created for each change. The flexibility of the code is also seen in the ability to refine the model without much computational effort, by simply changing the resolution setting. The postprocessing of the results also exhibits a good level of flexibility, with options available such as changing colour-bar axis limits, contour surface design and the level step.

7.5.2 Simplicity

The code designed follows the explicit two-dimensional finite difference method, which is inherently simple in its method. In each iteration of the code, each node designated in the cell is solved for explicitly. Once all nodes are solved for the temperature matrix is updated and the next time step runs using the new temperature matrix as its starting point. However, even though the code is not too complex it offers a high level of accuracy with regards to its results (Shabani and Biju, 2015). The user interface when using the code is also very straight forward (see Appendix C) and several parameters are automatically adjusted according to the user inputs. One example is the time interval, in traditional software, the user must define the step desired for the calculations, with this code the time step is automatically calculated using reference data inputted by the user.

7.5.3 Accuracy

Another impressive characteristic of this numerical model is its accuracy which was found to be very high, with results being accurate on average to within 95.7%. The accuracy of the numerical model was tested by comparing the maximum temperature values obtained from simulation to those taken from the University of Warwick's thermal images. The results from this accuracy investigation are shown in the Model Accuracy section. The worst test condition in terms of accuracy was the 5C discharge rate captured after 100 seconds, this test was 93% accurate. On the other hand, the most accurate testing conditions were under 3C discharge

captured after 800 seconds, this simulation was 98.7% accurate. Because of the model's overall accuracy, it is safe to say that the model is valid for further lithium battery investigations.

List of References

Becker, T. W. & Kaus, B. J. (2016). 'Numerical Modeling of Earth Systems', *An introduction to computational methods with focus on solid Earth applications of continuum mechanics. University of Southern California, Los Angeles. Lecture notes (224 pages), available online at http://www-udc.ig.utexas.edu/external/becker/Geodynamics557.pdf, accessed,* 9, p. 2017.

Chen, D., Jiang, J., Kim, G.-H., Yang, C. & Pesaran, A. (2016). 'Comparison of different cooling methods for lithium ion battery cells', *Applied Thermal Engineering,* 94, pp. 846-854.

Chen, K. (2013). *Heat Generation Measurements of Prismatic Lithium Ion Batteries.* University of Waterloo

Deng, Y., Feng, C., Jiaqiang, E., Zhu, H., Chen, J., Wen, M. & Yin, H. (2018). 'Effects of different coolants and cooling strategies on the cooling performance of the power lithium ion battery system: A review', *Applied Thermal Engineering,* 142, pp. 10-29.

Dombek, G., Nadolny, Z. & Marcinkowska, A. (2018). 'Effects of nanoparticles materials on heat transfer in electro-insulating liquids', *Applied Sciences,* 8(12), p. 2538.

Eberhard, M. & Tarpenning, M. (2006). 'The 21 st century electric car tesla motors', *Tesla Motors*.

Farid, M. M., Khudhair, A. M., Razack, S. A. K. & Al-Hallaj, S. (2004). 'A review on phase change energy storage: materials and applications', *Energy conversion and management,* 45(9-10), pp. 1597-1615.

Goli, P. & Balandin, A. A. (2014). Graphene-enhanced phase change materials for thermal management of battery packs. *In:* Fourteenth Intersociety Conference on Thermal and Thermomechanical Phenomena in Electronic Systems (ITherm), 2014. IEEE. pp. 1390-1393.

Halbright, R. & Dunn, M. (2010). 'Case Study: The Toyota Prius', *Managerial Marketing*.

Hosseinzadeh, E., Genieser, R., Worwood, D., Barai, A., Marco, J. & Jennings, P. (2018). 'A systematic approach for electrochemical-thermal modelling of a large format lithium-ion battery for electric vehicle application', *Journal of power sources,* 382, pp. 77-94.

Jabbari, M. (2019a). CAE/CFD LECTURE 6 – MATLAB LIVE. University of Manchester.

Jabbari, M. (2019b). Solver / Post-processing. University of Manchester.

Kellner, Q., Worwood, D., Barai, A., Widanage, W. D. & Marco, J. (2018). 'Duty-cycle characterisation of large-format automotive lithium ion pouch cells for high performance vehicle applications', *Journal of Energy Storage,* 19, pp. 170-184.

Liu, B., Jia, Y., Yuan, C., Wang, L., Gao, X., Yin, S. & Xu, J. (2019). 'Safety issues and mechanisms of lithium-ion battery cell upon mechanical abusive loading: a review', *Energy Storage Materials*.

Liu, H., Wei, Z., He, W. & Zhao, J. (2017). 'Thermal issues about Li-ion batteries and recent progress in battery thermal management systems: A review', *Energy conversion and management,* 150, pp. 304-330.

Lu, L., Han, X., Li, J., Hua, J. & Ouyang, M. (2013). 'A review on the key issues for lithium-ion battery management in electric vehicles', *Journal of power sources,* 226, pp. 272-288.

Ma, S., Jiang, M., Tao, P., Song, C., Wu, J., Wang, J., Deng, T. & Shang, W. (2018). 'Temperature effect and thermal impact in lithium-ion batteries: A review', *Progress in Natural Science: Materials International,* 28(6), pp. 653-666.

Maleki, H., Al Hallaj, S., Selman, J. R., Dinwiddie, R. B. & Wang, H. (1999). 'Thermal properties of lithium-ion battery and components', *Journal of The Electrochemical Society,* 146(3), p. 947.

Mei, W., Chen, H., Sun, J. & Wang, Q. (2018). 'Numerical study on tab dimension optimization of lithium-ion battery from the thermal safety perspective', *Applied Thermal Engineering,* 142, pp. 148-165.

Randall, T. (2016). 'Here's how electric cars will cause the next oil crisis', *Bloomberg, New York, accessed Mar,* 25, p. 2016.

Shabani, B. & Biju, M. (2015). 'Theoretical modelling methods for thermal management of batteries', *Energies,* 8(9), pp. 10153-10177.

Shafiee, S. & Topal, E. (2009). 'When will fossil fuel reserves be diminished?', *Energy policy,* 37(1), pp. 181-189.

Smil, V. (2016). *Energy transitions: global and national perspectives*: ABC-CLIO.

Wang, S. & Ni, R. (2019). 'Solving of Two-Dimensional Unsteady-State Heat-Transfer Inverse Problem Using Finite Difference Method and Model Prediction Control Method', *Complexity,* 2019.

Worwood, D., Kellner, Q., Wojtala, M., Widanage, W., McGlen, R., Greenwood, D. & Marco, J. (2017). 'A new approach to the internal thermal management of cylindrical battery cells for automotive applications', *Journal of Power Sources,* 346, pp. 151-166.

Wu, W., Yang, X., Zhang, G., Chen, K. & Wang, S. (2017). 'Experimental investigation on the thermal performance of heat pipe-assisted phase change material based battery thermal management system', *Energy Conversion and Management,* 138, pp. 486-492.

Xu, B., Oudalov, A., Ulbig, A., Andersson, G. & Kirschen, D. S. (2016). 'Modeling of lithium-ion battery degradation for cell life assessment', *IEEE Transactions on Smart Grid,* 9(2), pp. 1131-1140.

Appendices

Appendix A: Management of Project

Initial Plans

First Semester

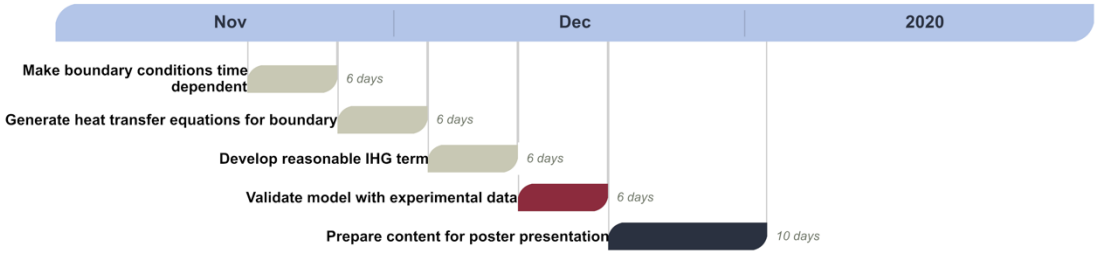

Second Semester

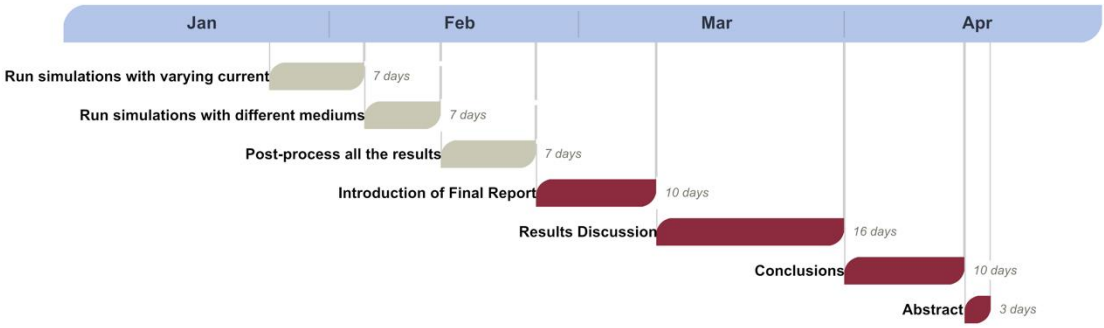

Updated Plan and Final Timeline

	ACTIVITY	PLAN START	PLAN DURATION	ACTUAL START	ACTUAL DURATION	PERCENT COMPLETE
1	Poster presentation preparation	1	2	1	2	100%
2	Remodeling internal domain nodes formula	2	1	3	2	100%
3	Developing transient capabilities	3	1	3	2	100%
4	Modelling heat transfer from the edges	3	1	4	1	100%
5	Creating identical colorbar	5	0.5	5	0.5	100%
6	Developing internal heat generation term	2	2	3	6	100%
7	Researching heat generation formulae	2	2	2	7	100%
8	Refining battery thermal characteristics	7	0.5	7	0.5	100%
9	Updating methodology for the final report	7	2	8	2	100%
10	Updating results for the final report	9	1	9	2	100%
11	Writing conclusions	9	1	9	2	100%
12	Writing limitations and recommendations	8	1	9	1	100%
13	Formating report	8	1	9	2	100%

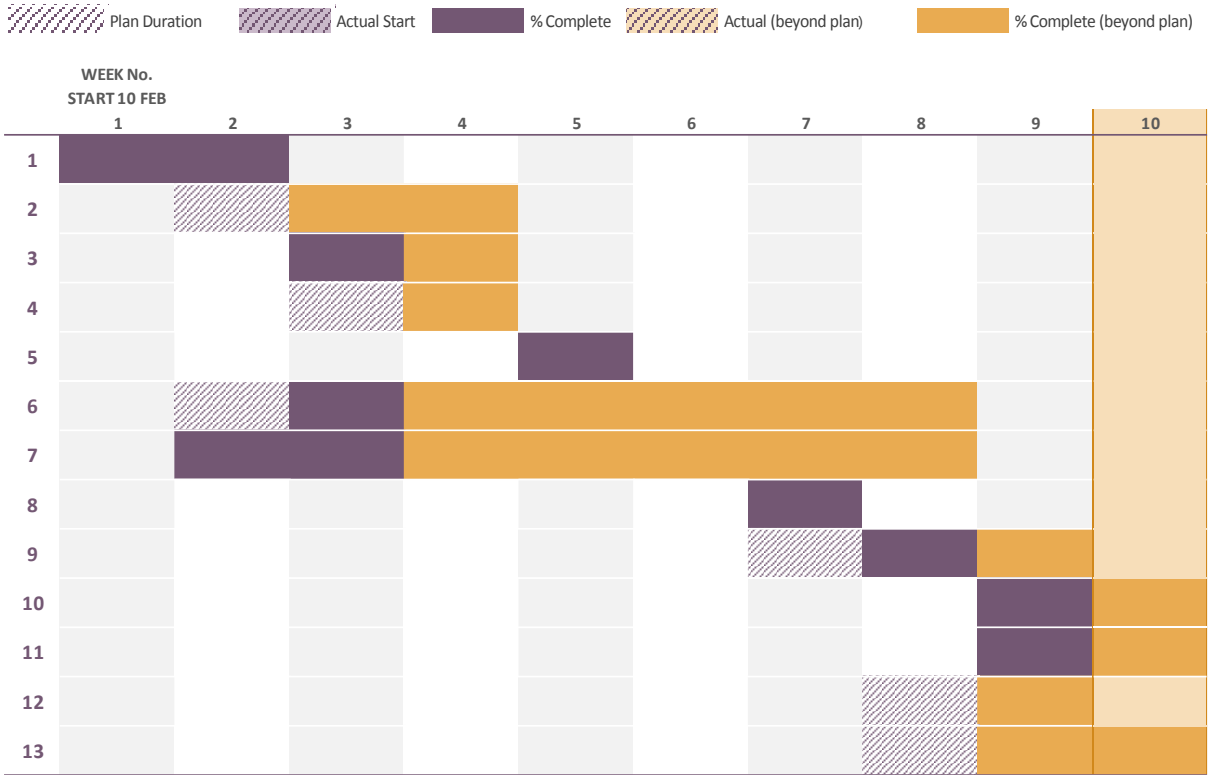

Reflections on the project plan

The biggest challenge faced with completing the original plan, was an inaccuracy in the results produced by the code during weeks 4-8. This time was very frustrating as the source of the problem could not be identified, so a fine comb through of the entire code was conducted to diligently inspect every equation. A significant amount of time was invested over these weeks as the problem with the results produced was not identified until around week 7 at which point it was found that the heat generation term used for the internal domain was the root cause. Originally, it was expected that the heat generation term would be worked on for two weeks, as it was believed that the equation used was correct. However, once work began it was clear that more research was needed to come up with an accurate solution. Once research began into this, several possible heat generation formulae were discovered in the literature. Some of these included entropy losses, electrical conductivity, and state of charge relationships. In the end the current density and internal resistance relationship was deemed the most suitable because of its simplicity to employ in MATLAB and its overall accuracy.

On the other hand, the plan was effective in the sense that it accurately predicted the time required to complete smaller sized tasks, and also it provided sufficient time as a buffer to react to unexpected problems.

Appendix B: MATLAB Numerical model code

Contents


```
clc,clear,close all
```

FDM solver for Laplace's equation in 2D

Settings

```
disp('Heat Conduction Equation solver for 2D Li-ion Battery')
disp(' ')

% Resolution
res = 120;                % Multiples of 15 only
left1 = res/15;
left2 = res*7/15;
right1 = res*8/15;
right2 = res*14/15;

% Width of domain
W = 0.2;

% Height of domain
L = 0.2;

% Grid spacing
gs = W / (res - 1);
```

Battery and Thermal Characteristics

```
k = 28;                          % thermal conductivity (W/m.K)
cp = 1100;                       % specific heat (J/kg K)
rho = 2551.7;                    % density (kg/m^3)
alpha = k/(cp*rho);              % alpha (1/sec)

BTMS=input('Is the BTMS convection based (1) or conduction based (2) ? ');
disp(' ')

C_rate = input('C rate (C) = '); % Charge/discharge rate

tfinal = input('Time Final (s) = ');

if BTMS==1
    h = input('Convective Heat Transfer coefficient (W/Km2) (Range:0 to 10e5) h =
');
    Bi = h*gs/k;
```

```
    term = Bi;
    n = h;
    name = 'h';
elseif BTMS==2
    k_cool=input('Conductive Heat Transfer coefficient (W/mK) (Range:0 to 27) k =
');
    term = (k_cool/k);
    n = k_cool;
    name = 'k';
end

R             = 1.33e-3 ;               % Ohm Resistance of the battery
R_tabP        = 3.37e-5 ;               % Ohm Resistance of the positive tab
W_tabP        = 0.08 ;                  % Positive tab width
R_tabN        = 3.48e-5 ;               % Ohm Resistance of the negative tab
W_tabN        = 0.08 ;                  % Negative tab width
Bat_cap       = 53.0 ;                  % Battery capacity (Ah)
I             = Bat_cap * C_rate ;      % Current of the battery: 5C * 53Ah
```

Time parameters

```
time = 0;

dt = 0.9*(gs^2)/(4*alpha);



Fo = (alpha*dt)/(gs^2);             % Fourier Number
```

Setting boundary conditions

```
Twall = 25;

phi = Twall*ones(res);
```

Sensor 1

```
X_sensor1 = 60;

Y_sensor1 = 60;

Tt1 = [time phi(Y_sensor1, X_sensor1)] ;    % Tt=[0 25]
```

Sensor 2

```
X_sensor2 = 10;

Y_sensor2 = 15;

Tt2 = [time phi(Y_sensor2, X_sensor2)] ;    % Tt=[0 25]
```

Heat Flux Calculation

```
qtab_neg = ((I^2)*R_tabN/(W_tabN^2));

qtab_pos = ((I^2)*R_tabP/(W_tabP^2));

% Creating a copy of phi
phi_old = phi;

tic
```

```
while time < tfinal
    for i=1:res
        for j=1:res
            % Bottom Left Corner
            if (i == 1 && j == 1)
                phi(i,j) = 0.5*(phi_old(i,j+1)+phi_old(i+1,j));

                % Bottom Right Corner
            elseif (i == res && j == 1)
                phi(i,j) = 0.5*(phi_old(i,j+1)+phi_old(i-1,j));

                % Top Left Corner
            elseif (i == 1 && j == res)

                phi(i,j) = 0.5*(phi_old(i,j-1)+phi_old(i+1,j));

                % Top Right Corner
            elseif (i == res && j == res)

                phi(i,j) = 0.5*(phi_old(i,j-1)+phi_old(i-1,j));

                % Bottom Edge
            elseif (j == 1)

                phi(i,j) = Fo*(phi_old(i-1,j) +2*phi_old(i,j+1) +phi_old(i+1,j)
+2*term*Twall +((1/Fo) -4 -(2*term))*phi_old(i,j));

                % Right Edge
            elseif (j ~= res && i == res)

                phi(i,j) = Fo*(phi_old(i,j+1) +2*phi_old(i-1,j) +phi_old(i,j-1)
+2*term*Twall +((1/Fo) -4 -(2*term))*phi_old(i,j));

                % Left Edge
            elseif (j ~= res && i == 1)

                phi(i,j) = Fo*(phi_old(i,j+1) +2*phi_old(i+1,j) +phi_old(i,j-1)
+2*term*Twall +((1/Fo) -4 -(2*term))*phi_old(i,j));

            end
        end
    end

    % Top Edge Gaps
    for i = [2:left1-1  left2+1:right1-1  right2+1:res-1]
        for j = res
            phi(i,j) = Fo*(phi_old(i-1,j) +2*phi_old(i,j-1) +phi_old(i+1,j)
+2*term*Twall +(1/Fo -4 -2*term)*phi_old(i,j));
        end
    end

    % Negative Tab
    for i = left1:left2
        for j = res
            phi(i,j) = Fo*(phi_old(i-1,j) +2*phi_old(i,j-1) +phi_old(i+1,j)
+2*gs*qtab_neg/387 +(1/Fo -4)*phi_old(i,j));
        end
    end

    % Positive Tab
    for i = right1:right2
        for j = res
            phi(i,j) = Fo*(phi_old(i-1,j) +2*phi_old(i,j-1) +phi_old(i+1,j)
+2*gs*qtab_pos/387 +(1/Fo -4)*phi_old(i,j));
        end
    end
```

```
    % Internal Domain
    for i = 2:res-1
        for j = 2:res-1
            qgen = ((I^2)*R)/(W*L*0.011);
            phi(i,j) = phi_old(i,j)+Fo*(phi_old(i,j+1)-4*phi_old(i,j) +phi_old(i,j-
1) +phi_old(i+1,j) +phi_old(i-1,j)) +(qgen*dt)/(rho*cp);
        end
    end

    phi_old = phi;
    time = time + dt;

    Tt1 = [Tt1 ; time phi(Y_sensor1, X_sensor1)] ; %% Tt1= [0 25 ; 0.1 25.1]
    Tt2 = [Tt2 ; time phi(Y_sensor2, X_sensor2)] ; %% Tt2= [0 25 ; 0.1 25.1]

end
toc
phi=transpose(phi);
```

Plot results

```
load colormap.mat

% Create meshgrid of plotting points
[xplot, yplot] = meshgrid(linspace(0, W, res), linspace(0, L, res));

% Find Temp Gradient
[ux, uy] = gradient(phi);
ux = -ux;
uy = -uy;

mag = sqrt(ux.^2 + uy.^2);
uxn = ux ./ mag;
uyn = uy ./ mag;

disp(' ')
disp('Value of Maximum Temperature (C)')
disp(max(max(phi)))
disp('Nodal Position of Maximum Temperature')
[X, Y] = find(ismember(phi, max(phi(:))));
fprintf('i = %d j = %d',Y,X)
disp(' ')
disp('Largest Temperature Difference (C)')
disp(max(max(phi))-min(min(phi)))

figure
quiver(xplot, yplot, uxn, uyn);
title('Normalised Heat Flux Field','interpreter','latex','Fontsize',14)
xlabel('x','interpreter','latex','Fontsize',14)
ylabel('y','interpreter','latex','Fontsize',14)
axis equal
axis tight

% Sensor 1
figure
plot(Tt1(1:end,1),Tt1(1:end,2));
title_text=sprintf('Temperature variation vs time at point (%d,%d)
',X_sensor1,Y_sensor1);
title(title_text,'interpreter','latex','Fontsize',14);
xlabel('Time (s)','interpreter','latex','Fontsize',14)
ylabel('Temperature (C)','interpreter','latex','Fontsize',14)

% Sensor 2
figure
plot(Tt2(1:end,1),Tt2(1:end,2));
title_text=sprintf('Temperature variation vs time at point (%d,%d)
',X_sensor2,Y_sensor2);
```

```
title(title_text,'interpreter','latex','Fontsize',14);
xlabel('Time (s)','interpreter','latex','Fontsize',14)
ylabel('Temperature (C)','interpreter','latex','Fontsize',14)

figure
contourf(xplot, yplot, phi,10);
colorbar
colormap(map)
caxis([26.8 64.2])
title_text=sprintf('%dC discharging for %ds, %s = %d ',C_rate,tfinal,name,n);
title(title_text,'interpreter','latex','Fontsize',14);
xlabel('x','interpreter','latex','Fontsize',14)
ylabel('y','interpreter','latex','Fontsize',14)
hcb=colorbar;
title(hcb,'Temperature','interpreter','latex','Fontsize',10)
view(2)
axis equal

file_name = sprintf('CR%d_tf%d ',C_rate,tfinal);
saveas(gcf,file_name,'pdf');
```

Published with MATLAB® R2018a

Appendix C: MATLAB User interface

Command Window

```
Heat Conduction Equation solver for 2D Li-ion Battery

Is the BTMS convection based (1) or conduction based (2) ? 1

C rate (C) = 5
Time Final (s) = 30
Convective Heat Transfer coefficient (W/Km2) (Range:0 to 10e5) h = 250
Elapsed time is 0.277821 seconds.

Value of Maximum Temperature (C)
   27.2693

Nodal Position of Maximum Temperature
i = 61 j = 61
Largest Temperature Difference (C)
    0.5791
```

Appendix D: Cooling Channel Add-on Code

The following code is added after the internal domain equations are written in the code in Appendix B.

```
% Hole
    for i = 49:71
        for j = 65:89
            k_hole = 0.133;
            rho_hole = 867;
            cp_hole = 1945;
            alpha2 = k_hole/(rho_hole*cp_hole);
```

```
            Fo2 = (alpha2*dt)/(gs^2);            % Fourier Number Coolant
            phi(i,j) = phi_old(i,j)+Fo2*(phi_old(i,j+1)-4*phi_old(i,j)
+phi_old(i,j-1) +phi_old(i+1,j) +phi_old(i-1,j));
        end
    end

    term2 = (k_hole/k);

    % Hole Left
    for i = 48
        for j = 64:88
            term2 = (k_hole/k);
            phi(i,j) = Fo*(phi_old(i,j+1) +2*phi_old(i-1,j) +phi_old(i,j-1)
+2*term2*phi_old(i+1,j) +((1/Fo) -4 -(2*term2))*phi_old(i,j));
        end
    end

    % Hole Right
    for i = 72
        for j = 64:88
            phi(i,j) = Fo*(phi_old(i,j+1) +2*phi_old(i+1,j) +phi_old(i,j-1)
+2*term2*phi_old(i-1,j) +((1/Fo) -4 -(2*term2))*phi_old(i,j));
        end
    end

    % Hole Bottom
    for i = 48:72
        for j = 64
            phi(i,j) = Fo*(phi_old(i-1,j) +2*phi_old(i,j-1) +phi_old(i+1,j)
+2*term2*phi_old(i,j+1) +(1/Fo -4 -2*term2)*phi_old(i,j));
        end
    end

    % Hole Top
    for i = 48:72
        for j = 88
            phi(i,j) = Fo*(phi_old(i-1,j) +2*phi_old(i,j+1) +phi_old(i+1,j)
+2*term2*phi_old(i,j-1) +((1/Fo) -4 -(2*term2))*phi_old(i,j));
        end
    end
```